Neuron

Article

Limited transmission of mixed convergent signals at the mouse retinogeniculate synapse

Highlights

- Optogenetic activation of ooDSGCs selectively drives DS dLGN neuron spiking
- Optogenetic activation of α-RGC selectively drives broadly tuned dLGN neurons
- dLGN cells can receive inputs from both RGC types, but often one predominates
- A minority of dLGN cells receive driving inputs from both RGC types

Authors

Takuma Sonoda, Qiufen Jiang, Ivan Jara-Marquez, Hannah Radell, Héctor Acarón Ledesma, Wei Wei, Chinfei Chen

Correspondence

chinfei.chen@childrens.harvard.edu

In brief

Sonoda, Jiang, et al. examine how mixed convergent retinal inputs shape signals in mouse dLGN. Using optogenetics, they find that individual retinal cell types largely dominate postsynaptic responses despite anatomical and functional convergence. This supports a labeled line model of signal transmission, suggesting more conserved principles across mammals than previously suggested.

Sonoda et al., 2025, Neuron *113*, 3260–3274
October 1, 2025
https://doi.org/10.1016/j.neuron.2025.06.015

CellPress

CellPress

Neuron

Article

Limited transmission of mixed convergent signals at the mouse retinogeniculate synapse

Takuma Sonoda,[1,2,4] Qiufen Jiang,[1,2,4] Ivan Jara-Marquez,[1,2] Hannah Radell,[1,2] Héctor Acarón Ledesma,[1,2] Wei Wei,[3] and Chinfei Chen[1,2,5,*]

[1]Department of Neurology, F.M. Kirby Neurobiology Center, Boston Children's Hospital, Boston, MA, USA
[2]Department of Neurobiology, Blavatnik Institute, Harvard Medical School, Boston, MA, USA
[3]Department of Neurobiology, The University of Chicago, Chicago, IL, USA
[4]These authors contributed equally
[5]Lead contact
*Correspondence: chinfei.chen@childrens.harvard.edu
https://doi.org/10.1016/j.neuron.2025.06.015

SUMMARY

There are two broad modes of information transfer in the brain: the labeled line model, where neurons relay inputs they receive, and the mixed tuning model, where neurons transform different inputs. In the visual pathway, information transfer between retinal ganglion cells (RGCs) and dorsal lateral geniculate nucleus (dLGN) neurons is viewed as a labeled line. However, recent work in mice demonstrated that different RGC types, encoding distinct visual features, converge onto a dLGN neuron, raising the question of how the dLGN transforms visual information. Using optogenetics, we activated distinct RGC populations and measured dLGN neuron spiking *in vivo*. We found that visual response properties of strongly driven dLGN neurons largely match properties of the activated RGC population. While *in vitro* dual-opsin experiments demonstrate that strong functional convergence from distinct RGC types does occur at modest frequencies, our data largely support a labeled line model of retinogeniculate information transfer in mice.

INTRODUCTION

In the primary pathway mediating visual perception, retinal ganglion cells (RGCs, see Table S1 for all abbreviations) synapse onto thalamocortical (TC) neurons in the dorsal lateral geniculate nucleus (dLGN), which then transmit information to the primary visual cortex (V1).[1–4] Classic functional studies in the cat visual system demonstrated that TC neurons receive strong "driver-like" inputs from a few RGCs that are capable of evoking spiking.[5–11] These findings have established the prevailing view that TC neurons function as simple relays of retinal input. However, several of these studies also noted the presence of weak connections, indicating that TC neurons can receive weak functional inputs from numerous RGCs.[7–10,12–15] In fact, most connected RGC-TC neuron pairs do not exhibit a 1:1 relationship in terms of spiking, as would be predicted by a simple labeled line model.[5,7–9] Therefore, these studies raised the intriguing possibility that signals from multiple RGCs are combined in the dLGN.

Recent work in the mouse visual system has reignited interest in the idea that TC neurons might function as integrators rather than simple relays of RGC input. Studies examining the RGC inputs onto dLGN neurons have shown that more than 10 RGCs can innervate a single dLGN neuron[16–18] and that these RGCs can consist of different types.[19–21] These studies have been interpreted by many as evidence that mouse visual processing is significantly different from that of higher mammals. Indeed, extensive work has revealed important species differences, including the relative abundance of RGC types, lamination patterns in the dLGN, and receptive field properties in mice compared with higher mammals.[4,22–24] However, there has been a fundamental difference in the approaches used to understand visual processing in different species. For example, seminal cat and primate studies largely focused on dLGN neuron spiking responses using *in vivo* recording approaches,[5–7,25,26] whereas work in mice has taken advantage of genetic tools and other modern approaches with higher resolution, sensitivity, and specificity. Therefore, conclusions drawn about different species could largely be a product of the levels of analyses used to study visual processing.

To narrow the gap between approaches used between species, we assessed the contribution of distinct RGC types to the spiking output of dLGN neurons in mice. We utilized optogenetics to activate subsets of RGCs *in vivo* and recorded resulting spiking activity in postsynaptic dLGN neurons. We found that the visual response properties of dLGN neurons that reliably spiked in response to optogenetic stimulation matched the properties of the RGC population being activated. Our findings suggest that despite the convergence of multiple RGC types onto a dLGN neuron, one type tends to dominate the postsynaptic spiking

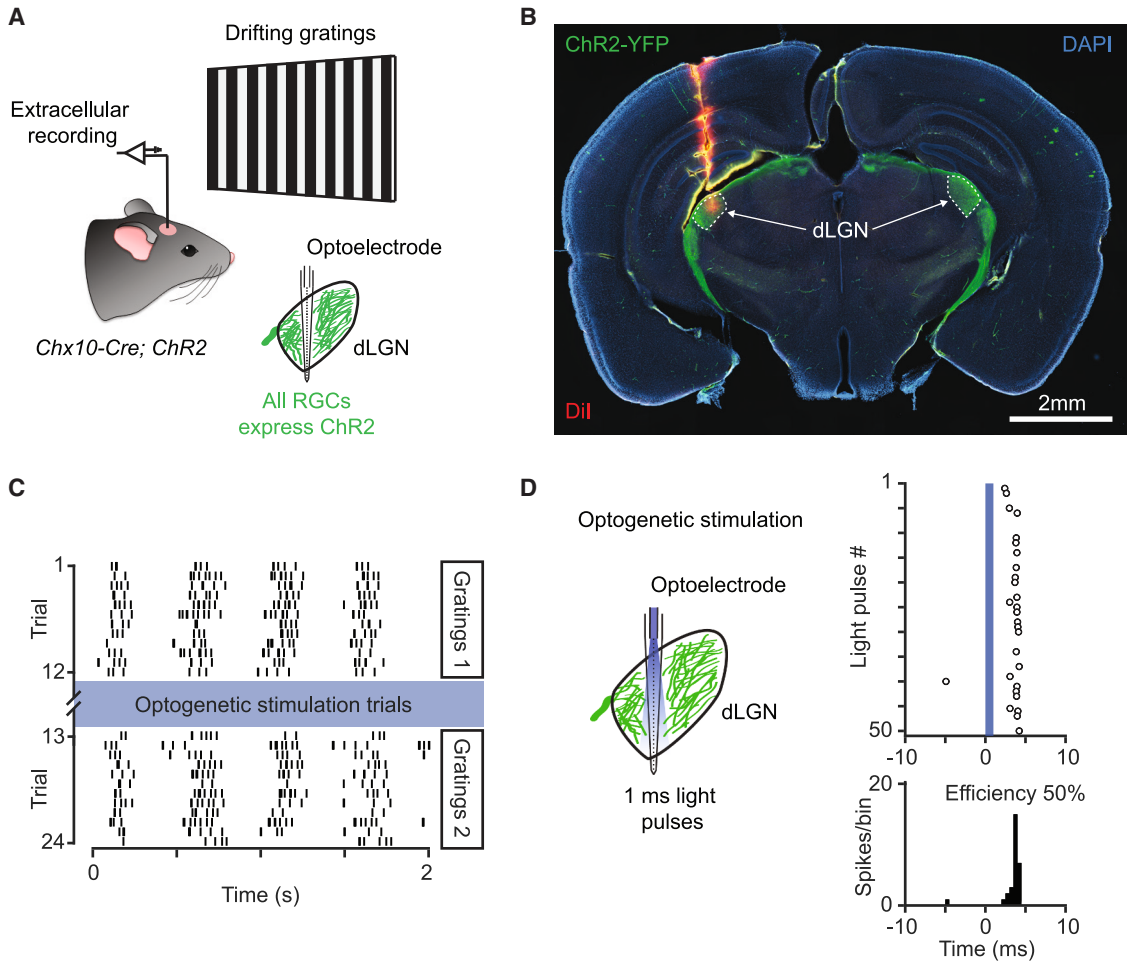

Figure 1. Measuring visual responses and functional inputs from RGCs simultaneously in dLGN neurons *in vivo*

(A) *In vivo* extracellular dLGN recordings were performed in *Chx10-Cre*; *ChR2* mice in which all retinal cells, including RGCs, express ChR2. The axons of RGCs expressing ChR2 were optogenetically activated using silicon probes with optical fibers attached (optoelectrodes). This approach enabled simultaneous recording of dLGN neuron responses to visual stimuli and optogenetic activation of RGC axons *in vivo*.

(B) Coronal brain section collected from a *Chx10-Cre*; *ChR2* mouse after *in vivo* dLGN recording. Green signals are RGC axons labeled in *Chx10-Cre*; *ChR2* mice. The electrode tract trajectory was labeled with DiI (red).

(C) Raster plot of responses to drifting gratings from an example dLGN neuron. Drifting gratings stimuli were presented before and after optogenetic stimulation trials (blue) to ensure recording stability.

(D) Responses of the same dLGN neuron in (C) to 1 ms optogenetic stimulation of RGC axons. The top raster plot shows spiking responses over a 20 ms window, with time 0 indicating the onset of the light pulse. The bottom plot is a peristimulus time histogram of spiking activity in 0.5 ms bins. This neuron exhibited an opto-spike efficiency of 50% with a latency of 4 ms.

response. We also examined functional convergence of two distinct RGC types *in vitro* using a dual-opsin approach. When comparing synaptic strengths of the two distinct RGC types onto a given TC neuron, the likelihood of a cell receiving strong inputs from both populations is low, consistent with a labeled line model. Our results suggest that despite species differences, the principles underlying information transfer in the retinogeniculate pathway remain largely conserved. They also show that conclusions drawn about neural circuits can vastly differ depending on the level of analysis and emphasize the importance of interpreting anatomy with function. Taken together with other published studies, our study raises future questions regarding the purpose of the weak convergent RGC inputs.

RESULTS

Optogenetic stimulation of RGC axons in the dLGN *in vivo*

We first sought to examine connections between specific RGC populations and dLGN neurons by utilizing optogenetics *in vivo*. This approach involved measuring responses of the same dLGN neurons to (1) drifting sine-wave gratings and (2) optogenetic activation of a subset of RGC axons (Figure 1A)—enabling us to functionally classify dLGN neurons that receive driving input from specific RGC populations. We validated this approach by making *in vivo* dLGN recordings in anesthetized *Chx10-Cre; ChR2* mice: a mouse line in which all RGCs express

channelrhodopsin-2 (ChR2)[17,27] (Figures 1A and 1B). Multisite silicon probes with an attached optical fiber (optoelectrodes) were used to make *in vivo* extracellular recordings from dLGN neurons while optogenetically activating RGC axons expressing ChR2 (Figure 1A). Gratings were presented before and after a block of optogenetic trials to ensure that responses to optogenetic stimulation were not due to unstable recording conditions (Figure 1C). Only units that exhibited reliable visual responses before and after optogenetic stimulation were included for analysis (see STAR Methods).

During optogenetic stimulation trials, we activated RGC axons by delivering 1 ms light pulses at 5 Hz while animals viewed a dark screen. We quantified the extent to which spiking was evoked in postsynaptic dLGN neurons in response to RGC axon stimulation by binning spiking responses to optogenetic stimulation into 0.5 ms intervals to create a peristimulus time histogram (Figure 1D). We defined opto-spike efficiency by summing the spikes in the peak interval with spikes in the two adjacent intervals, dividing this number by the total number of light pulses delivered, and multiplying by 100 to convert to a percentage.

On average, the first pulse of the 5 Hz pulse train elicited the most reliable spiking with an opto-spike efficiency of 38.8% ± 30.4% (mean ± SD, $n = 52$ visually responsive units) and delay of 4.4 ± 0.9 ms (Figure S1A), consistent with a monosynaptic response.[9] No spiking was elicited in response to optical stimulation in Cre-negative *ChR2* animals ($n = 7$ units; Figure S1B). Opto-spike efficiency was not significantly different in units recorded in the superficial versus deeper half of dLGN, indicating effective stimulation spread of RGC axons across the entire depth of dLGN (Figures S1C and S1D). These experiments demonstrate the feasibility of measuring responses to visual stimuli and optogenetic activation of RGC axons in the same dLGN neuron *in vivo*.

Optogenetic activation of ooDSGCs elicits robust spiking in a subset of DS dLGN neurons

We next investigated the extent to which activation of a single RGC population can drive spiking in postsynaptic dLGN neurons *in vivo*. We utilized *Cart-IRES2-Cre* mice crossed to *Ai32* mice (*Cart-Cre; ChR2*) to express ChR2 in on-off direction-selective RGCs (ooDSGCs). We have previously shown that this cross specifically labels ooDSGC inputs to the dLGN.[20] We broadly categorized the visual responses of dLGN neurons to drifting sine-wave gratings as broadly tuned (BrT, 296/456 of visually responsive units), axis selective (AS, 111/456 units), direction selective (DS, 30/456 units), or suppressed by contrast (Sbc, 19/456) (Figure 2A). BrT neurons respond equally to gratings moving in all directions, AS neurons respond to gratings moving along a specific axis of motion, DS neurons respond to gratings moving in a specific direction, and Sbc neurons suppress their baseline firing in response to gratings (Figure 2A). The proportions of these functional categories were largely consistent with those reported by previous studies recording dLGN responses in similar conditions.[28–30] DS dLGN neurons were defined as units exhibiting a direction-selectivity index (DSI) > 0.33, and AS neurons were defined as units exhibiting a DSI < 0.33 and an axis-selectivity index (ASI) > 0.33 (Figure 2C) (see STAR Methods).

Optogenetic activation of Cart-Cre$^+$ axons in the dLGN elicited robust spiking, defined as an opto-spike efficiency greater than 40% (Figures 2B and 2D), in only a small subset of dLGN units (3.5%). Among these, 75% were DS (Figures 2A–2D and S2B). We selected the 40% cutoff because DS neurons showed a clear divergence in opto-spike efficiency at this cutoff. Lowering the opto-spike efficiency cutoff incrementally from 40% to 10% increased the proportion of BrT neurons, potentially suggesting weaker inputs from ooDSGCs to BrT dLGN neurons (Figure S2B). However, these findings can also be explained by non-selective labeling, as the *Cart-Cre* line also labels a small fraction of other RGC types.[20] Importantly, DS dLGN neurons were significantly more responsive to Cart-Cre$^+$ inputs than other RGC-driven dLGN neurons, regardless of the opto-spike efficiency threshold used to define reliably driven neurons (Figure S2A). This specificity for DS dLGN neurons also did not depend on the DSI cutoff used for classifying DS dLGN neurons (0.33) (Figure 2E). These results suggest a high degree of specificity in retinogeniculate connectivity when examined at the level of functional connections capable of driving spiking *in vivo*.

Functional properties of DS neurons in the dLGN

Our results also show that there are DS dLGN neurons that do not respond to Cart-Cre$^+$ input activation (Figure 2D), raising the question of what properties differentiate DS neurons that are reliably driven by Cart-Cre$^+$ inputs from those that are not. In our experiments, we measured dLGN neuron responses to two sets of drifting grating stimuli with different spatial frequencies: the first set of gratings being coarser (0.04 cycles/degree) and the other finer (0.16 cycles/degree). The temporal frequency of both sets of gratings was fixed at 2 cycles/s; therefore, coarser gratings also moved faster than finer gratings (50 degrees/s versus 12.5 degrees/s). Notably, DS dLGN neurons could be subdivided by their preference for these two sets of gratings (Figure 3A). We computed a gratings preference index to quantify the preference of each DS unit for these two sets of gratings. The gratings preference index ranges from −1 to 1, with values closer to −1 indicating a stronger preference for fast, coarse gratings, while values closer to 1 indicate a stronger preference for slow, fine gratings (Figure 3C) (see STAR Methods). DS dLGN neurons exhibited a bimodal distribution in gratings preference index (Figure 3C; Hall and York calibration of Silverman's test, $p = 0.008$), while BrT and AS dLGN neurons exhibited broader, unimodal distributions favoring fast, coarse gratings (Figure S3; Hall and York calibration of Silverman's test, $p = 0.582$ for BrT and $p = 0.356$ for AS).

DS dLGN neurons that prefer slower, finer gratings (gratings preference index > 0), which we termed type 1 DS, responded robustly to optogenetic activation of Cart-Cre$^+$ inputs (Figures 3B and 3D) and primarily resided in the superficial half of dLGN (Figures S4A–S4C). Conversely, DS dLGN neurons that preferred faster, coarser gratings (gratings preference index < 0), termed type 2 DS, did not respond to optogenetic activation of Cart-Cre$^+$ input (Figures 3B and 3D). The spatial frequency and speed preferences of type 1 DS dLGN neurons are consistent with responses of ooDSGCs described previously.[31,32] We directly confirmed this by imaging calcium responses of ooDSGCs of the retinas of *Cart-Cre*; *GCaMP6f*

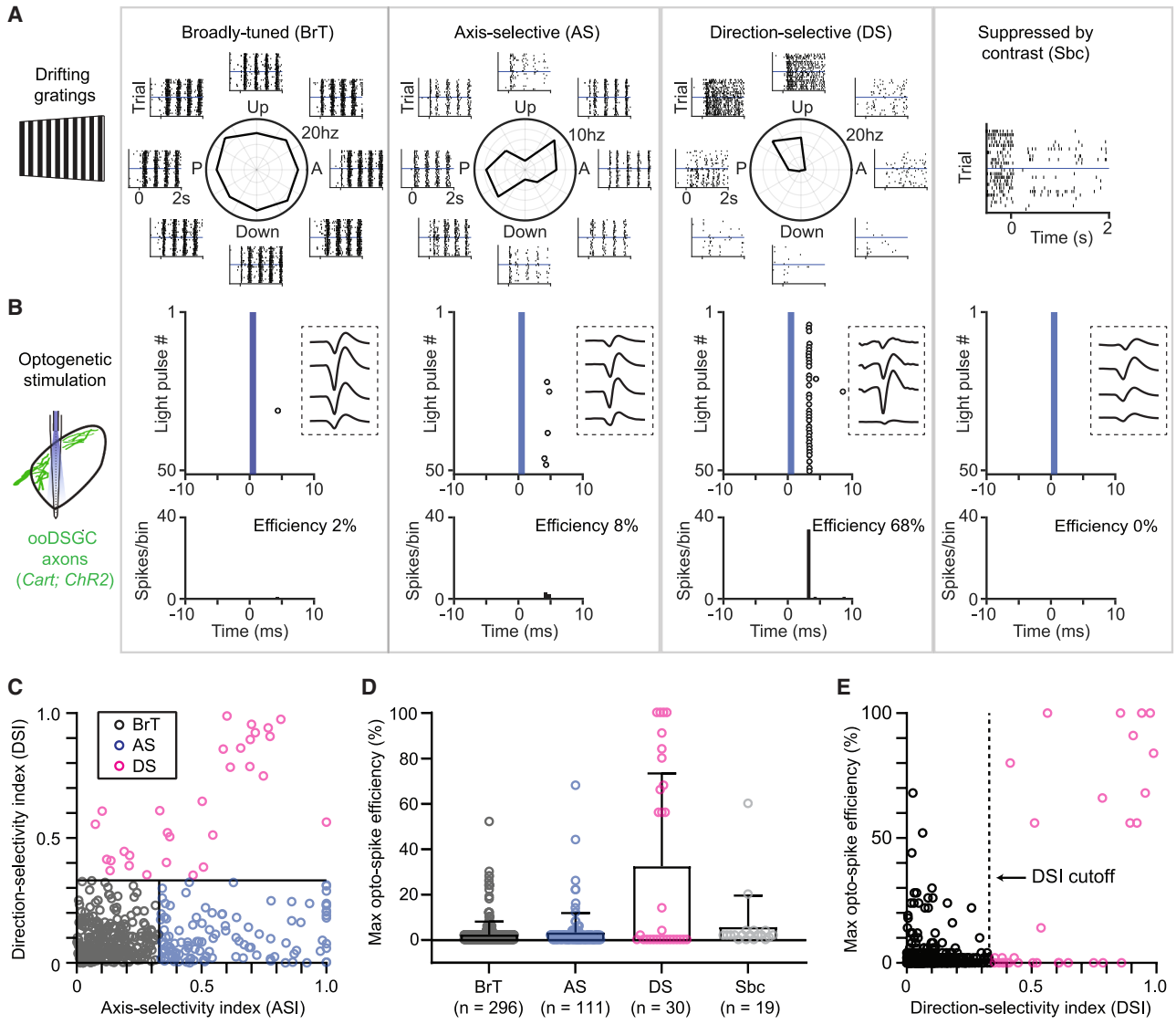

Figure 2. Visual responses of dLGN neurons receiving driving inputs from Cart-Cre$^+$ RGCs

(A) Example responses of broadly tuned (BrT), axis-selective (AS), direction-selective (DS), and suppressed by contrast (Sbc) dLGN neurons to drifting gratings. Polar plots in the center represent average firing rate in response to gratings moving in 8 different directions. Raster plots surrounding each polar plot each show spiking activity in response to drifting gratings moving in a single direction across multiple trials. Time 0 denotes the onset of the drifting grating stimulus. Responses to gratings moving in a single direction are displayed for the Sbc dLGN neuron. A, anterior; P, posterior.

(B) Responses of the same neurons in (A) to optogenetic activation of Cart-Cre$^+$ RGC inputs. The top raster plots show spiking responses to 1 ms light pulses over a 20 ms window. Open circles represent spikes. The onset of optogenetic stimulation occurs at time 0 and is represented by the solid blue box. The insets surrounded by dotted boxes are the average spike waveforms of each example neuron recorded across multiple recording sites on the multielectrode array. The bottom plots are peristimulus time histograms of spiking activity in 0.5 ms bins.

(C) Scatter plot of ASI and DSI plotted for every visually responsive dLGN neuron with reliable spiking across trials, excluding Sbc neurons. BrT neurons (gray) were classified as cells with DSI < 0.33 and ASI < 0.33, AS neurons (blue) were classified as cells with ASI > 0.33 and DSI < 0.33, and DS (pink) neurons were classified as cells with DSI > 0.33.

(D) Max opto-spike efficiency of different functional classes in response to optogenetic activation of Cart-Cre$^+$ RGC input. Data are from single units pooled from 49 *Cart-Cre*; *ChR2* animals. Bar plots and error bars represent mean ± SD.

(E) Max opto-spike efficiency as a function of DSI. The dotted vertical line depicts the DSI cutoff used to classify DS neurons in this study (0.33).

mice to the same drifting gratings stimuli (Figure 4A). ooDSGCs exhibited the same preference for slower, finer (0.16 cycles/degree) gratings (Figures 4B and 4C)—matching the preference of postsynaptic DS dLGN neurons that are strongly driven by optogenetic activation of Cart-Cre$^+$ RGCs (Figure 4). Additionally, the direction preferences of type 1 DS dLGN neurons strongly driven by Cart-Cre$^+$ inputs largely conformed to the vertical axis (Figure S5), consistent with our previous study showing that

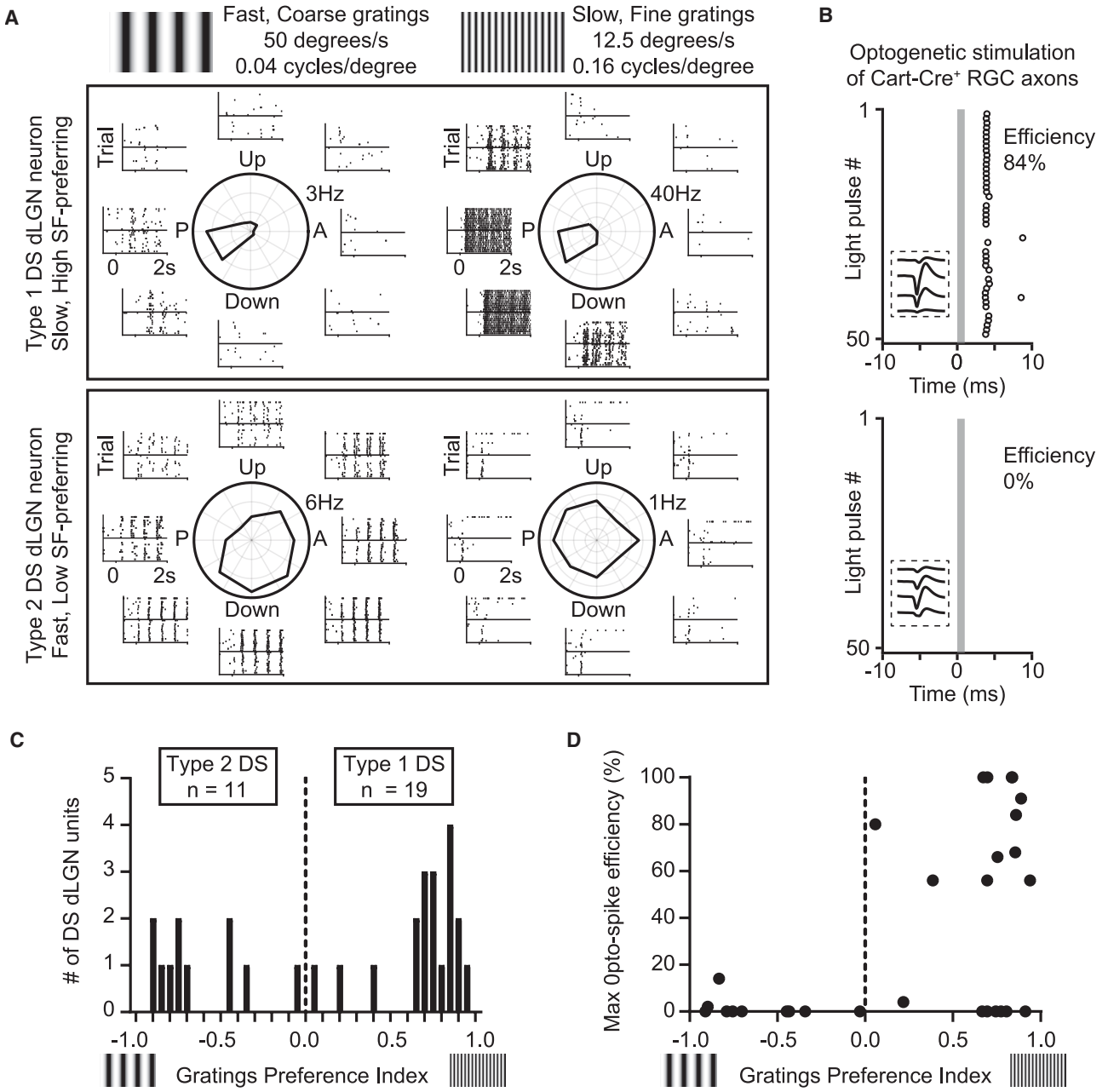

Figure 3. Cart-Cre$^+$ inputs onto different types of DS neurons in the mouse dLGN

(A) Example responses of DS dLGN neurons to two types of gratings. The left panels show responses to fast, coarse gratings, and the right panels show responses to slow, fine gratings. The top panels are example responses of a DS dLGN neuron that prefers slow, fine gratings (type 1). The bottom panels show responses of a DS dLGN neuron that prefers fast, coarse gratings (type 2).

(B) Raster plots showing responses of the same dLGN neuron in (A) to 1 ms optogenetic stimulation of RGC axons. Time 0 marks the onset of optogenetic stimulation. The insets surrounded by dotted boxes are the average spike waveforms of each neuron recorded across multiple recording sites on the multi-electrode array.

(C) Histogram of gratings preference index plotted for DS dLGN neurons recorded in *Cart-Cre*; *ChR2* mice. Gratings preference index was computed by taking the difference between responses to the two different gratings divided by the sum of the responses (see STAR Methods). Values ranging from 0 to −1 indicate a preference for fast, coarse gratings, and values ranging from 0 to 1 indicate a preference for slow, fine gratings. The distribution of gratings preference index was significantly multimodal (Hall and York calibration of Silverman's critical bandwidth test, $p = 0.008$). Units with a gratings preference index greater than 0 were classified as type 1 DS, and units with a gratings preference index less than 0 were classified as type 2 DS.

(D) Max opto-spike efficiency as a function of gratings preference index. Note that units strongly driven by Cart-Cre$^+$ inputs exhibited gratings preference indexes greater than 0 (i.e., they are type 1 DS).

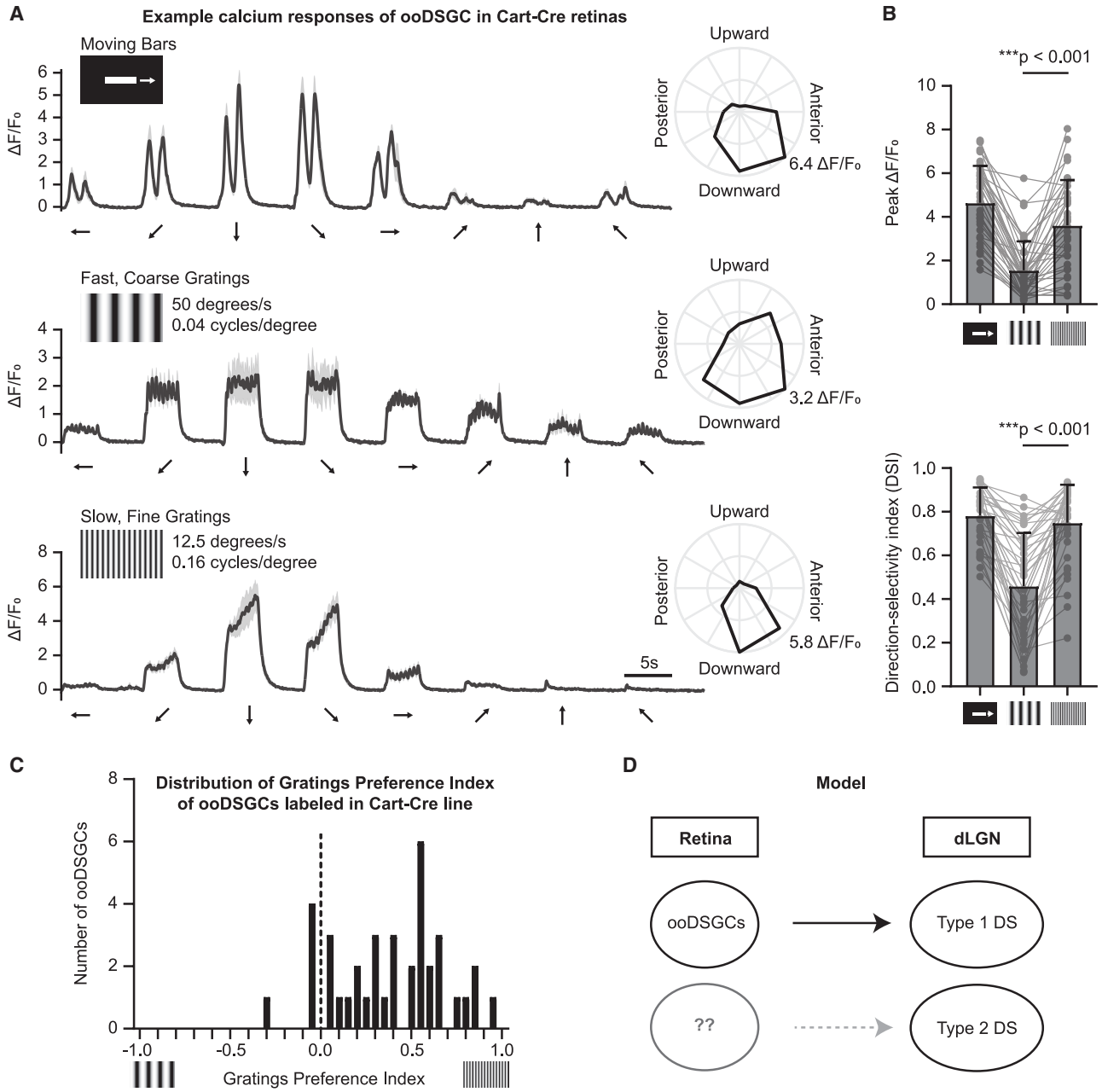

Figure 4. Responses of ooDSGCs to drifting gratings of different spatial frequencies

(A) Example calcium responses of an ooDSGC labeled in *Cart-Cre*; *GCaMP6f* mice. The cell was presented with bars and drifting gratings moving in different directions. Black lines represent the mean response averaged across 4 trials, and the gray lines represent standard error. Polar plots to the right are peak $\Delta F/F_0$ responses to stimuli moving in different directions. Note lower response amplitudes in response to faster, coarser-grating stimuli.

(B) Grouped data of peak $\Delta F/F_0$ (top) and DSI (bottom) to different visual stimuli. ooDSGCs exhibited significantly larger responses to finer 0.16 cycles/degree gratings, like type 1 DS dLGN neurons (Figure 3). n = 38 cells. Bar plots and error bars represent mean ± SD. ***$p < 0.001$, paired t test.

(C) Histogram of gratings preference index plotted for ooDSGCs labeled in *Cart-Cre*; *GCaMP6f* mice.

(D) Working model showing how type 1 DS dLGN neurons receive strong inputs from ooDSGCs.

ooDSGCs labeled in Cart-Cre$^+$ animals largely preferred vertical (upward and downward) motion.[20] These results support the idea that ooDSGC responses are largely inherited by a subset of dLGN neurons (Figure 4D).

Optogenetic activation of α-RGCs elicits reliable spiking in broadly tuned dLGN neurons

Our results suggest that DS inputs to the dLGN exhibit a high degree of specificity. But does this specificity generalize to other

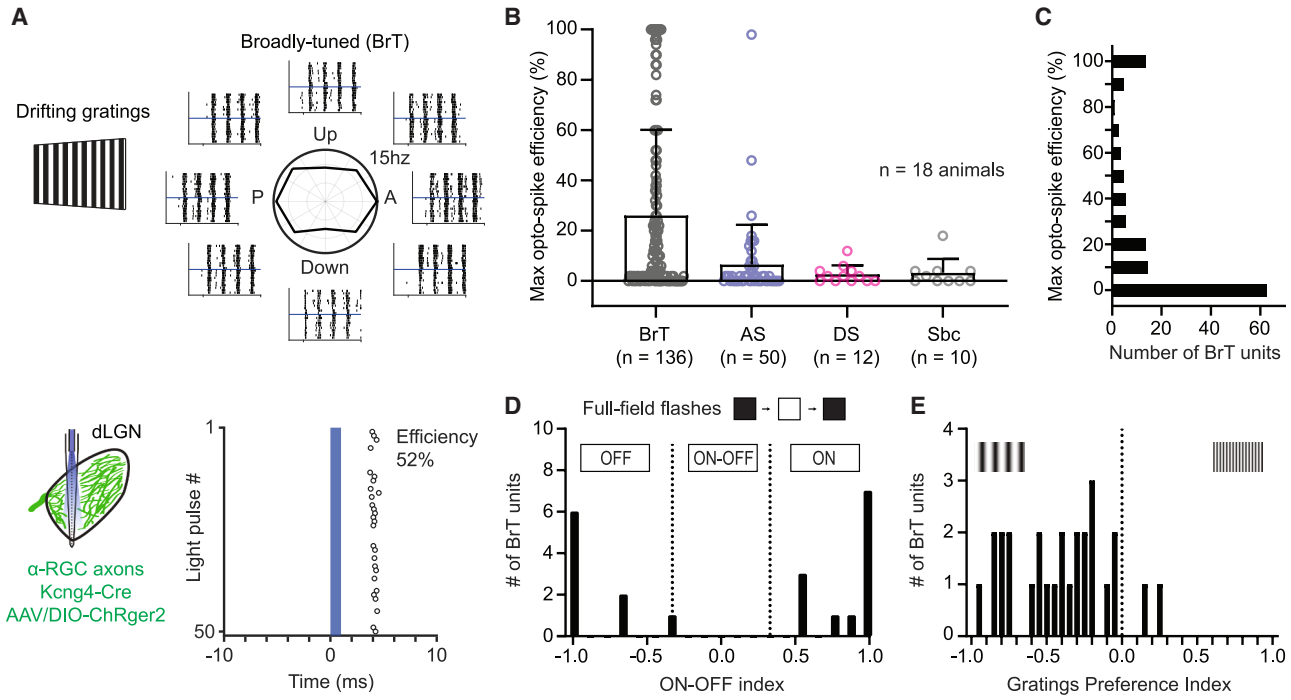

Figure 5. Visual responses of dLGN neurons receiving driving inputs from Kcng4-Cre$^+$ RGCs

(A) ChRger2, a ChR variant, was expressed in α-RGCs by injecting AAVs into *Kcng4-Cre* mice. The top plots are responses of a broadly tuned dLGN neuron to drifting gratings moving in 8 directions. The bottom raster plot shows spiking responses of the same neuron in the top panel to optogenetic activation of Kcng4-Cre$^+$ RGC input over a 20 ms window. The onset of optogenetic stimulation occurs at time 0 and is represented by the solid blue box.

(B) Max opto-spike efficiency of different functional classes in response to optogenetic activation of Kcng4-Cre$^+$ RGC input. Bar plots and error bars represent mean ± SD. BrT dLGN neurons are the primary population of dLGN neurons to receive driving input from Kcng-Cre$^+$ RGCs (see also Figure S2).

(C) Histogram of max opto-spike efficiency of BrT units recorded in *Kcng4-Cre* mice. Data are the same as those plotted for BrT units from in (B). The distribution was significantly multimodal (Hall and York calibration of Silverman's critical bandwidth test, $p < 0.001$).

(D) Histogram of on-off index measured in response to 1 s full-field flashes. Data are from BrT dLGN units that received strong Kcng4-Cre$^+$ inputs (opto-spike efficiency > 40%) ($n = 21$ units).

(E) Histogram of gratings preference index plotted for BrT dLGN units that received strong Kcng4-Cre$^+$ inputs (same units as those plotted in D).

RGC types? To address this, we utilized *Kcng4-Cre* mice to label α-RGCs, which are BrT.[33–35] We targeted Kcng4-Cre$^+$ RGCs by making eye injections of adeno-associated virus (AAV)-CAG-DIO-ChRger2-YFP, which drives Cre-dependent expression of a ChR variant, ChRger2,[36] between P20 and P30, and performed *in vivo* recordings between P60 and P120. We performed eye injections of AAVs instead of crossing to *ChR2* reporter mice because this cross results in labeling of dLGN neurons (data not shown). BrT dLGN neurons were significantly more reliably driven compared with other functional types in response to optogenetic activation of Kcng4-Cre$^+$ inputs (Figures 5A, 5B, S2C, and S2D).

Further analysis of BrT neurons that were reliably driven by Kcng4-Cre$^+$ RGCs, defined as exhibiting an opto-spike efficiency of greater than 40%, showed clear ON or OFF responses to full-field luminance flashes (Figure 5D). Only 1 of 21 neurons that were responsive to full-field flashes had an ON-OFF response, as defined as exhibiting responses with an on-off index between −0.33 and 0.33 (see STAR Methods) (Figure 5D). Because α-RGCs consist of only ON and OFF types,[35,37] these results suggest that there is no strong functional convergence of ON and OFF α-RGC inputs onto a single dLGN neuron and that information encoded by α-RGCs is also relayed to the visual cortex. Additionally, BrT dLGN neurons that reliably spiked in response to Kcng4-Cre$^+$ RGC activation also exhibited a stronger preference for fast, coarse gratings (Figure 5E), consistent with responses of α-RGCs to drifting gratings.[38] Thus, when examined at the level of inputs capable of driving spiking *in vivo*, the mouse retinogeniculate synapse exhibits a high degree of specificity similar to higher mammals.

Examining functional convergence of α-RGC and ooDSGC inputs *in vitro*

Our *in vivo* experiments show that activating functionally defined populations of RGCs elicits reliable spiking in a small subset of dLGN neurons, the majority of which match functional properties of the optogenetically activated RGC population. These results largely support a model where dLGN neurons inherit retinal tuning features. However, it is unclear whether dLGN neurons are capable of being driven by multiple distinct RGC types. Therefore, we sought to directly measure convergent inputs from different RGC types onto a single dLGN neuron using a dual-opsin strategy, which involves independently activating two

distinct RGC populations and measuring their maximal synaptic drive onto the same dLGN neurons.

We expressed a red-shifted opsin in α-RGCs by eye injection of *Kcng4-Cre* mice with AAVs that drive Cre-dependent expression of ChrimsonR-tdTomato[39] (Figure 6A). To label an RGC population distinct from α-RGCs, we co-injected AAVs that drive expression of a blue-shifted opsin, CatCh,[40] in ooDSGCs under the control of the ProD1 promoter (Figure 6A). ProD1 is a synthetic promoter that targets expression to a subset of ooDSGCs.[41] Importantly, most CatCh-GFP$^+$ RGCs (termed "ProD1$^+$," 98%) exhibit no overlap with ChrimsonR-tdTomato$^+$ RGCs (termed "Kcng4-Cre$^+$") (Figures 6B and 6C). Co-immunostaining for cocaine- and amphetamine-regulated transcript neuropeptide (CART), a marker of ooDSGCs,[42,43] shows that the majority (72%) of ProD1-labeled RGCs are CART immunoreactive (CART-IR) and that 27% of CART-IR RGCs are ProD1$^+$ (Figures 6C and 6D). Therefore, while ProD1$^+$ RGCs primarily represent a subset of ooDSGCs and are not entirely pure, they are a distinct RGC population from Kcng4-Cre$^+$ RGCs, providing a useful tool to study the convergence of distinct RGC populations onto single dLGN neurons.

In the dLGN, the axons of Kcng4-Cre$^+$ and ProD1$^+$ RGCs exhibit distinct projection patterns in coronal sections (Figures 6E and 6F). In anterior coronal sections, ProD1$^+$ axons localize to the superficial region of dLGN (within 100 μm away from the optic tract) and extend to deeper portions (<400 μm) in more posterior sections (Figures 6E and 6F). Kcng4-Cre$^+$ inputs are not prominent but are still observed in the superficial region across the anterior-posterior axis and overlap with ProD1$^+$ axons over a more expanded area in posterior coronal sections (Figures 6E and 6F). These termination patterns are consistent with previous studies of ooDSGCs and α-RGCs[20,44–46] and show that there are regions in the dLGN that receive inputs from both populations.

To preserve the integrity of the optic tract, we utilized parasagittal slices for voltage clamp recordings.[47] In parasagittal slices, the terminal endings of ProD1$^+$ and Kcng4-Cre$^+$ RGC axons overlap in the ventral-posterior area (Figure 6G$_i$). Higher resolution images of this area reveal intermingling of ProD1$^+$ and Kcng4-Cre$^+$ boutons (Figure 6G$_{ii-iii}$), raising the possibility that these two different RGC types might converge onto the same dLGN neurons. We thus targeted TC neurons in the ventral-posterior area of dLGN for patch clamp recording (Figure 7A). Alexa Fluor 647 (Alexa 647) was added to the internal solution to fill the neurons for post hoc morphological analysis. 3D reconstructions revealed the proximity of both Kcng4-Cre$^+$ and ProD1$^+$ axonal terminals to the proximal dendrites of postsynaptic dLGN neurons (Figures 7A and S6).

We then measured the optically evoked excitatory postsynaptic currents (oEPSCs) in response to activation of two distinct RGC populations by using different light wavelengths (Figure 7B). As CatCh can be activated by blue light (470 nm) and ChrimsonR is sensitive to both orange (>600 nm) and blue light, synaptic responses from Kcng4-Cre$^+$ inputs were evoked by a pulse of orange light (Figure 7C$_{ii}$; see STAR Methods). Prolonged stimulation of orange light will drive ChrimsonR into the desensitized state, rendering it transiently unresponsive to blue light.[48] We took advantage of this property to obtain the response to ProD1$^+$ inputs by delivering blue light stimulation immediately following 250 ms of orange light illumination (Figures 7B and 7C; see STAR Methods). The amplitude of blue light-evoked currents is comparable to that of summed responses to Kcng4-Cre$^+$ and ProD1$^+$ inputs obtained with a desensitizing orange light prepulse (Figure S7A; $p = 0.53$, Wilcoxon matched-pairs signed rank test), suggesting that this approach is reliable in quantifying the synaptic strengths from the two distinct RGC populations. Moreover, the average amplitude of the oEPSCs did not significantly differ when comparing Kcng4-Cre$^+$ and ProD1$^+$ input-evoked responses for each cell across the entire population (Figure S7B; $p = 0.57$, paired t test), indicating that this approach is reliable in quantifying the synaptic strengths from the two distinct RGC populations.

A total of 54 TC neurons were recorded from 20 mice for dual-opsin recordings. Examination of individual TC neurons showed that TC neurons can receive a wide range of input amplitudes (0–6 nA; Figure 7D), in agreement with previous work using electrical and optical stimulation of RGC inputs.[17,49,50] This is unlikely to be attributed to differential labeling of these two populations in the retina, since relative proportions of virally labeled Kcng4-Cre$^+$ and ProD1$^+$ RGCs were consistent across animals (Figure S7C). To quantify the extent to which each RGC population contributes to the summed synaptic response, we computed a contribution index (CI) for cells with detectable functional input (51/54 cells). CI is defined as the ratio of the difference between the responses of the two RGC populations ($R_{ProD1} - R_{Kcng4}$) to their summed response ($R_{ProD1} + R_{Kcng4}$) (Figure 7E). A CI of 0 indicates equal inputs from both RGC types, whereas values close to −1 or 1 reflect a predominance in Kcng4-Cre$^+$ or ProD1$^+$ RGC inputs, respectively (see STAR Methods). The distribution of CI shows that the majority of TC neurons (70.6%, 36/51 cells) exhibited CI values below –0.9 or above 0.9, indicating that one RGC population accounted for more than 95% of the summed response (Figure 7E). These results indicate that even in regions innervated by both RGC populations, most TC neurons receive a summed contribution of inputs from predominantly one population.

We then focused on the subset of TC neurons receiving strong inputs, defined as those with at least one RGC population contributing to a synaptic response exceeding 0.6 nA—a threshold previously shown to drive spiking *in vitro*.[51] In this subset of TC neurons (11/51 cells), the CI distribution was similar to that observed for the overall population: 8 of 11 cells (72.7%) had CI values below –0.9 or above 0.9, whereas 3 of 11 (27.3%) displayed relatively balanced input strength from both RGC populations (Figures 8A and 8B). Notably, the 3 cells with CI between –0.9 and 0.9 received strong inputs (≥0.6 nA) from both populations (Figure 8C), indicating they can be driven by distinct RGC populations.

Given that factors such as brain state and neuromodulation may alter the EPSC amplitude threshold required for spiking,[51,52] we further examined how the proportion of cells receiving strong, suprathreshold inputs from both populations changes with varying amplitude thresholds for a "strong" input (Figure 8D). These analyses revealed that the proportion of TC neurons that receive strong inputs from both populations does not change dramatically with different thresholds (Figure 8D). Thus, when analyzing synaptic inputs from two populations of RGCs, we find functionally relevant mixing of RGC inputs in a few but appreciable proportion of

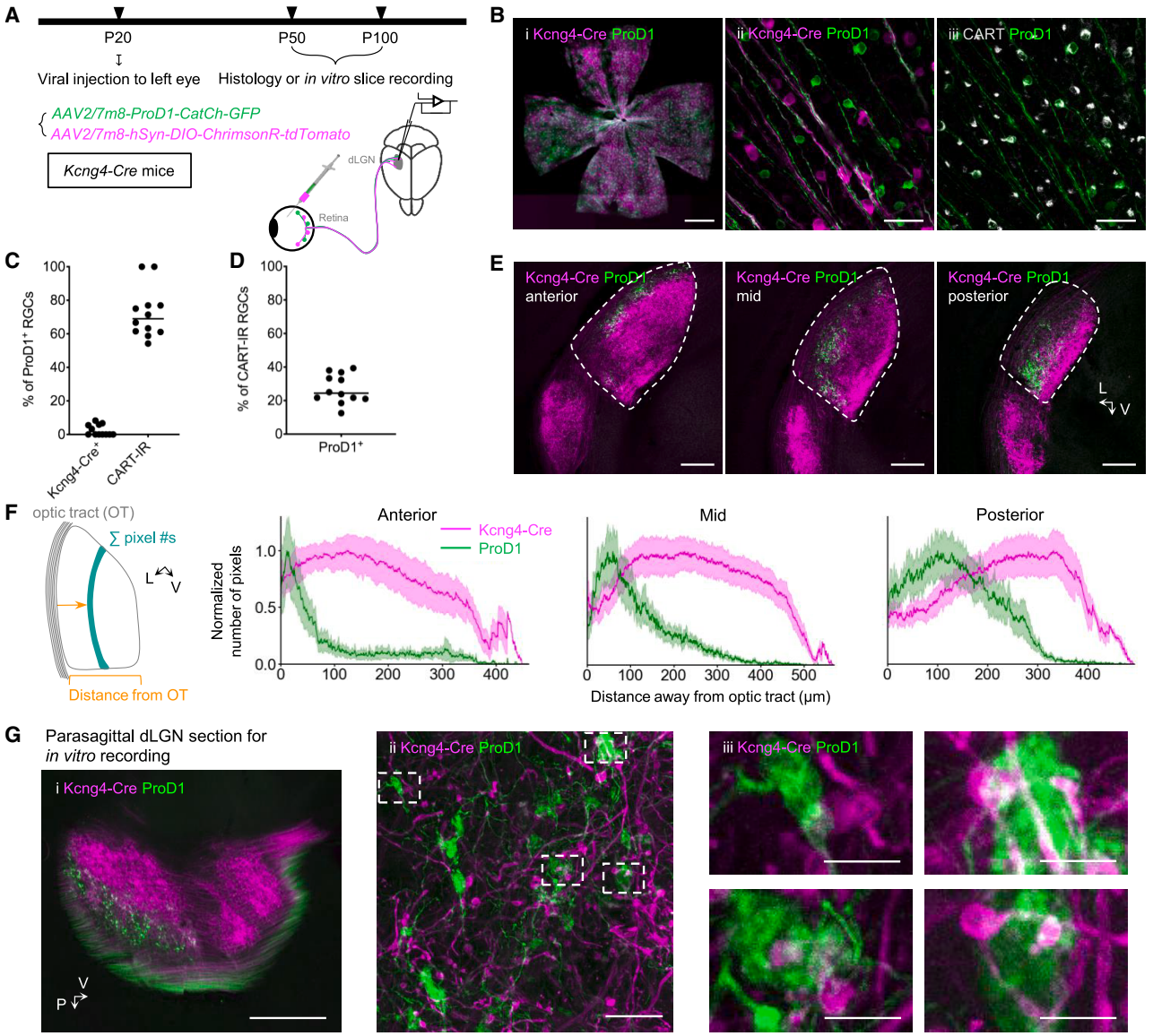

Figure 6. Viral strategy for simultaneously labeling α-RGCs and ooDSGCs in the retina

(A) Strategy and experimental timeline for labeling Kcng4-Cre$^+$ and ProD1$^+$ RGCs in the retina. ~P20 *Kcng4-Cre* mice were eye injected with viruses that drive Cre-dependent expression of ChrimsonR-tdTomato and Cre-independent *ProD1* promoter-driven expression of CatCh-GFP to label α-RGCs and ooDSGCs, respectively. Histology and *in vitro* slice recordings were performed between P50 and P100.

(B) Images of Kcng4-Cre$^+$ and ProD1$^+$ RGCs labeled in the retina. (B_i) Low-magnification image of a whole-mount retina with Kcng4-Cre$^+$ and ProD1$^+$ RGCs labeled. Scale bar, 200 μm. (B_{ii}) High-magnification image of the ganglion cell layer (GCL) of the retina showing ProD1$^+$ (green) and Kcng4-Cre$^+$ (magenta) RGCs exhibiting no overlap. Scale bar, 50 μm. (B_{iii}) High-magnification image of the GCL showing a high degree of overlap between ProD1$^+$ and CART-immunoreactive (CART-IR) RGCs (a marker of ooDSGCs). Scale bar, 50 μm.

(C) Proportion of ProD1$^+$ RGCs that co-localize with Kcng4-Cre$^+$ or CART-IR RGCs. The majority of ProD1$^+$ RGCs (72%) are CART-IR and exhibit minimal overlap with Kcng4-Cre$^+$ RGCs (2.5%).

(D) Proportion of CART-IR RGCs labeled by *ProD1*-promoter-driven viral expression of CatCh-GFP. (C and D) n = 12 mice.

(E) Coronal brain sections of the dLGN taken at different levels along the anterior-posterior axis. L, lateral); V, ventral. Scale bar, 200 μm.

(F) Distribution of Kcng4-Cre$^+$ and ProD1$^+$ signals summed along the medial-dorsal to lateral-ventral axis as a function of distance away from the optic tract (OT). Left: schematic for the measurement of summed pixels. The vertical teal area shows accumulated pixels along the binned line parallel to the OT at a distance (orange arrow) from the OT. Right: distribution of Kcng4-Cre$^+$ and ProD1$^+$ signals from representative anterior, mid, and posterior regions of dLGN.

(G) Axonal terminations of Kcng4-Cre$^+$ and ProD1$^+$ RGCs in a parasagittal dLGN section used for *in vitro* slice physiology recordings. (G_i) Low-magnification image of the parasagittal dLGN with Kcng4-Cre$^+$ and ProD1$^+$ inputs labeled. Scale bar, 500 μm. (G_{ii}) High-magnification overlay of Kcng4-Cre$^+$ and ProD1$^+$ boutons in ventral-posterior area of dLGN. Scale bar, 20 μm. (G_{iii}) Potential clusters containing both Kcng4-Cre$^+$ and ProD1$^+$ boutons. Images were taken from areas indicated by dashed line boxes in (G_{ii}). Scale bar, 5 μm.

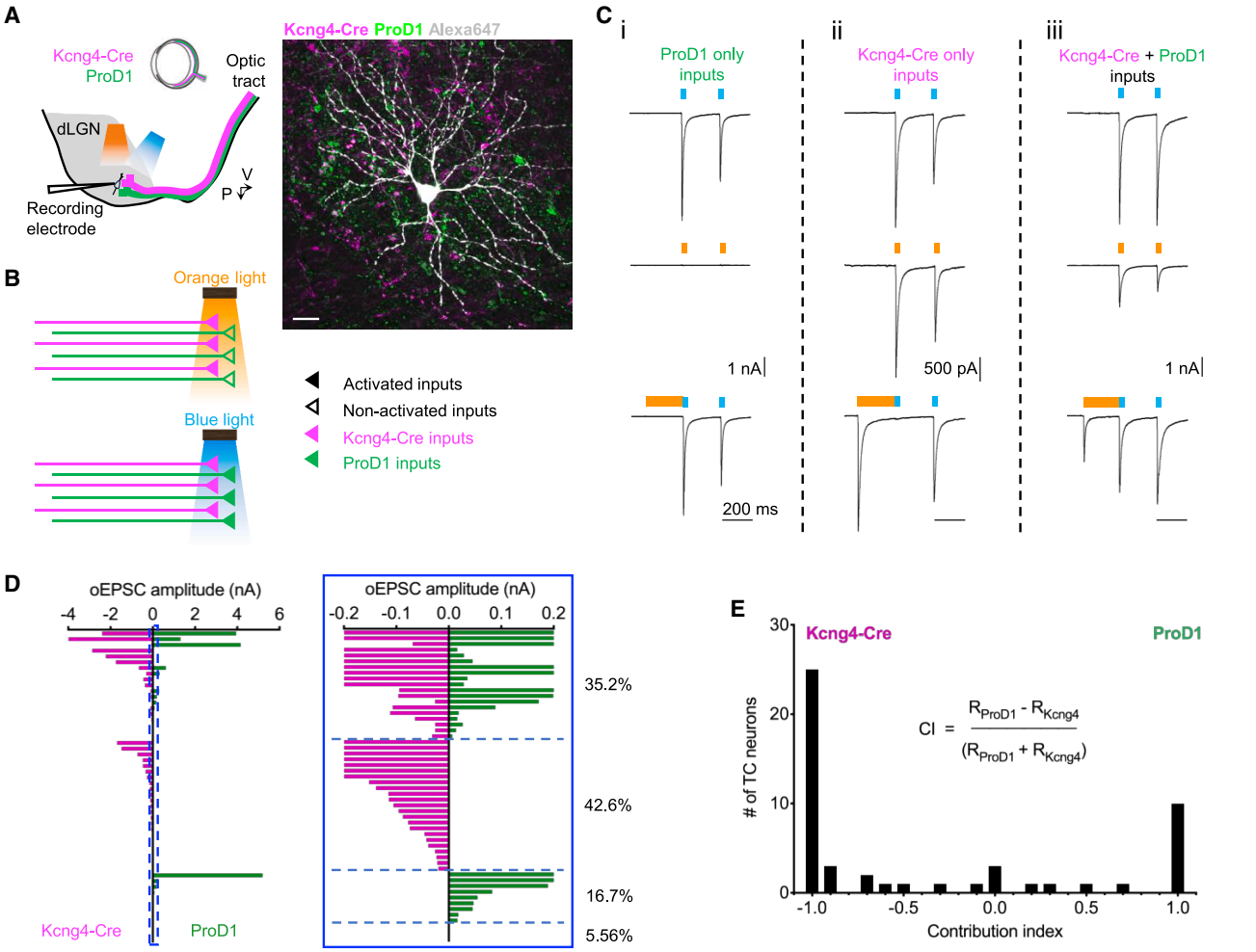

Figure 7. Skewed dLGN neuron responses to optogenetic activation of Kcng4-Cre$^+$ and ProD1$^+$ RGC inputs

(A) Recording from TC neurons in ventral-posterior dLGN. Left: schematic showing recording configuration used for optical stimulation of Kcng4-Cre$^+$ and ProD1$^+$ inputs. Parasagittal sections of dLGN were prepared for patch clamp recording. Blue (470 nm) and orange (>600 nm) full-field light stimulations were used for optogenetic activation. P, posterior; V, ventral. Right: image showing an example TC neuron filled with Alexa Fluor 647 (Alexa647) to visualize dendritic morphology. Proximal dendrites were in close proximity to Kcng4-Cre$^+$ and ProD1$^+$ terminals. Scale bar, 20 μm. See also Figure S6.

(B) Schematic depicting activation of Kcng4-Cre$^+$ and ProD1$^+$ inputs with different wavelengths of light. Filled triangles represent activated terminals, while open triangles represent non-activated terminals. CatCh is expressed in ProD1$^+$ axons (green) and can be activated by blue light (470 nm). ChrimsonR is expressed in Kcng4-Cre$^+$ axons (magenta) and is activated by both orange (>600 nm) and blue light.

(C) Examples of TC neurons that receive ProD1$^+$ only input (C_i), Kcng4-Cre$^+$ only input (C_{ii}), and both Kcng4-Cre$^+$ and ProD1$^+$ inputs (C_{iii}). To isolate the synaptic responses from the two populations of inputs, Kcng4-Cre$^+$ inputs were evoked by a pulse of orange light (1 ms). Because blue light activates both inputs, 250 ms of orange light illumination was first delivered to desensitize ChrimsonR in Kcng4-Cre$^+$ axons, rendering them transiently insensitive to optostim, followed by a 0.2 ms of blue light pulse to isolate the synaptic response from ProD1$^+$ inputs.

(D) Paired responses to activation of Kcng4-Cre$^+$ (negative, magenta) and ProD1$^+$ (positive, green) RGC inputs. Right: expanded view of dashed blue line box from the left for inputs smaller than 0.2 nA. $n = 54$ cells, 20 mice. Of all recorded neurons, 35.2% (19/54) responded to activation of both inputs, 42.6% (23/54) only to activation of Kcng4-Cre$^+$ inputs, 16.7% (9/54) only to activation of ProD1$^+$ RGCs, and 5.56% (3/54) did not respond to either population.

(E) Frequency distribution of contribution index (CI). The majority of TC neurons (70.6%, 36/51 cells) receive selective input from Kcng4-Cre$^+$ or ProD1$^+$ RGCs ($|CI| \geq 0.9$).

TC neurons (20%–30%). However, the majority of TC neurons exhibit functional selectivity for one RGC population.

DISCUSSION

Previous studies using serial electron microscopy (EM),[16,18] single-rabies tracing,[19] and presynaptic imaging[21] suggested there is significant mixing of retinal signals in the mouse dLGN. However, whether this anatomical convergence results in meaningful functional transformation remains unclear. While functional and modeling approaches[13,17,20,53] suggested that only 1–3 of these many RGC inputs are strong enough to influence postsynaptic spiking, our study is the first to directly assess information transfer in the dLGN by simultaneously measuring functional

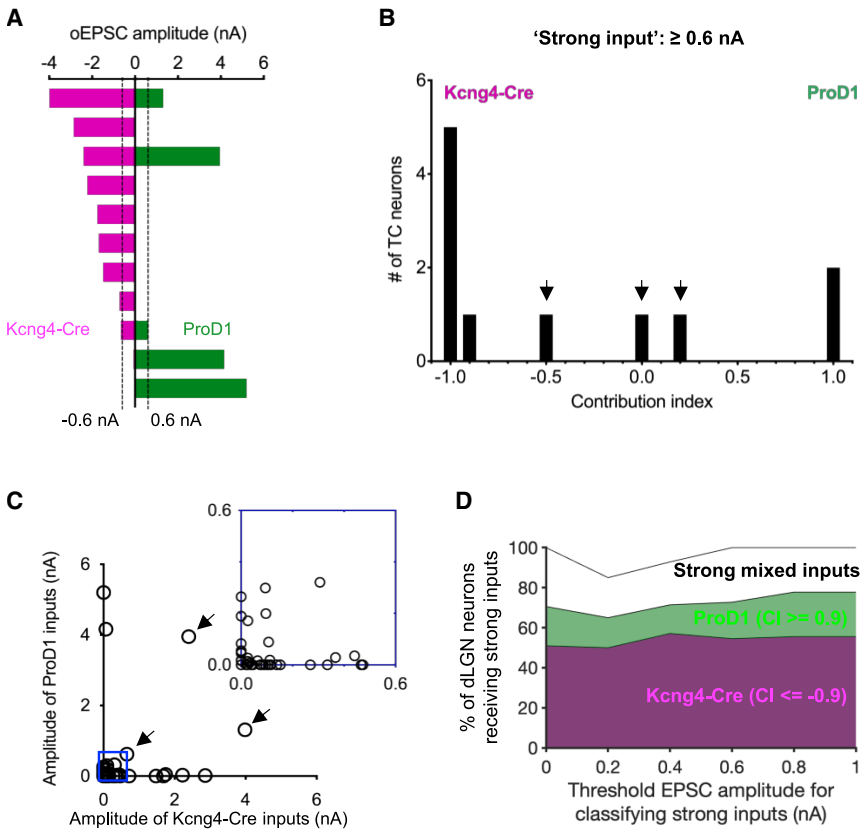

Figure 8. Limited strong convergence between Kcng4-Cre$^+$ and ProD1$^+$ RGC inputs

(A) Paired responses to activation of Kcng4-Cre$^+$ (negative) and ProD1$^+$ (positive) RGC inputs in TC neurons receiving strong inputs from at least one RGC population. Vertical dashed line indicates (±) 0.6 nA EPSC amplitude, the threshold we use for strong inputs.

(B) Frequency distribution of CI for TC neurons receiving strong inputs from at least one RGC population. Arrows indicate the responses with equivalent contribution from Kcng4-Cre$^+$ and ProD1$^+$ inputs (|CI| < 0.9).

(C) Scatter plot of responses to activation of Kcng4-Cre$^+$ and ProD1$^+$ inputs. Arrows indicate the same responses as in (B), showing TC neurons receiving strong inputs from both Kcng4-Cre$^+$ and ProD1$^+$ RGCs. Inset shows the responses smaller than 0.6 nA, zoomed from the blue box.

(D) Stacked area graph showing the percentage of cells receiving dominant input from Kcng4-Cre$^+$ RGCs (magenta), dominant input from ProD1$^+$ RGCs (green), and strong mixed inputs from both populations (white). The percentages do not change significantly with changes in the EPSC threshold amplitude defining a "strong" input.

connectivity and dLGN neuron spiking output in the same preparation. We focused on strong functional connections that elicit spiking, as has been the convention in functional studies of higher mammals. We report that at this level of analysis, the mouse retinogeniculate pathway is more consistent with a labeled line model in which the dLGN relays retinal signals to V1. Therefore, our findings bring the field back into alignment with prior work in other species and provide clarity about the role of the thalamus in visual processing. These findings should not diminish the contribution of convergent inputs to visual processing but prompt further questions regarding their purpose. Broadly, our results underscore the importance of interpreting cutting-edge approaches, such as rabies tracing and 3D EM reconstruction, in the context of function.

The mouse dLGN transmits information in a labeled line model

Our previous dLGN slice recordings in *Cart-Cre; ChR2* mice showed that while 79.6% (74/93 cells) of TC neurons receive functional Cart-Cre$^+$ RGC input, only 24.3% (18/74 cells) of these cells receive strong inputs capable of driving spiking.[20] It was unclear whether these strong inputs dominate the postsynaptic response and result in DS being relayed to the visual cortex. This was not feasible to directly test in slice due to the lack of molecular or morphological markers to identify functional dLGN neuron types. In this study, we use an *in vivo* approach to directly measure the functional output of dLGN neurons that receive strong inputs from Cart-Cre$^+$ RGCs. If dLGN neurons receive strong inputs from different RGC types, we expect the visual responses of dLGN neurons driven by Cart-Cre$^+$ RGC inputs to be complex. However, we found that the primary population of dLGN neurons that are driven by Cart-Cre$^+$ inputs, the type 1 DS neurons, share functional properties with DS Cart-Cre$^+$ RGCs (Figures 2, 3, 4, and S5). Despite the variability in the preferred directions of type 1 DS neurons corresponding to downward motion (Figure S5), they are largely consistent with those of Cart-Cre$^+$ RGCs.[20] This variability in preferred directions likely reflects alignment of ooDSGC preferred directions with translatory optic flow fields, which vary by retinotopic location.[43] Taken together, our results suggest that RGCs of the same type provide strong inputs to dLGN neurons, which then relay these signals to the visual cortex.[44,54–57]

We observed a population of DS dLGN neurons that appear to lack a strong driver input from Cart-Cre$^+$ RGCs ("type 2 DS," Figure 3). The fact that these type 2 DS dLGN neurons do not spike in response to Cart-Cre$^+$ input activation is consistent with their distinct stimulus preferences for gratings that do not optimally activate ooDSGCs (Figure 4). However, we cannot rule out the possibility that the excitability of Cart-Cre$^+$ RGC axons innervating type 2 DS dLGN neurons has different anatomical or electrical properties that make them less excitable by optogenetic stimulation. Regardless, these results raise the question of how DS is computed or refined in type 2 DS dLGN neurons. It is possible that DS is driven by other DS RGC types, such as F-mini RGCs or ON-DSGCs; although, the speed tuning of F-mini and ON-DS RGCs suggests that this is unlikely.[31,58–60] Another possibility is that type 2 DS responses are computed locally via a disynaptic pathway involving interneurons. The

existence of distinct populations of DS dLGN neurons indicates the dLGN may send multiple forms of DS signals to the visual cortex, as suggested by a previous study.[61]

We conducted experiments in *Kcng4-Cre* mice to determine whether our results in *Cart-Cre; ChR2* animals generalize to inputs from other RGC types. *Kcng4-Cre* mice primarily label α--RGCs, which are BrT. Importantly, we find that the primary population of dLGN neurons that are driven by activation of Kcng4-Cre$^+$ inputs are also BrT (Figure 5), further generalizing the labeled line model for retinogeniculate processing to other RGC types. Moreover, Kcng4-Cre$^+$ inputs primarily target the "core" region of the dLGN, while Cart-Cre$^+$ inputs primarily innervate more superficial regions (Figure 6). This suggests that our results are applicable to both regions of the dLGN. As more genetic tools are developed to manipulate specific RGC types, it will be important to explore how information encoded by other RGC types shapes visual responses of dLGN neurons.

Signal transformation in the dLGN

Our results generally support a labeled line model for transmission of retinal signals to the visual cortex. However, they leave room for the possibility that certain TC neurons transmit more than one line of information. Results from this and previous studies[17,20] indicate that most RGC inputs to TC neurons are subthreshold and not capable of driving spiking in mice. However, recent studies have highlighted that factors such as arousal and brain state differentially alter the calcium responses of axonal boutons of specific RGC types in the dLGN.[62,63] Thus, we speculate that with changes in the relative weights of convergent RGC inputs, the response properties of TC neurons may change. Furthermore, neuromodulators such as serotonin can have opposing effects on presynaptic RGC terminals and postsynaptic TC neuron excitability, where it suppresses specific RGC types coupled with TC neuron depolarization.[62,64] These changes could lead to transmission of information from unsuppressed RGC types, resulting in weaker inputs becoming more prominent in different contexts or brain state.[65–68] *In vivo* recordings in this study, like those in cats, were conducted in anesthetized animals, limiting the influence of behavioral states on spiking output in our studies. An interesting avenue for future research will be to understand how specific connections are altered in different contexts.

Importantly, weak connections between RGCs and dLGN neurons are not a feature specific to the mouse retinogeniculate system, as these inputs have been described both at the functional and anatomical level in cats and primates.[5,7–9,69] Mixed convergent RGC inputs have also been observed, albeit infrequently.[11,69] In the cat visual system, divergent retinal signals have been shown to provide inputs of varying strengths to TC neurons, which may function to create more continuous representations of visual space[10,70,71] and serve as a mechanism for creating ensembles of TC neurons that can reliably influence cortical spiking in response to certain visual stimuli.[8,9,15] Weak inputs have also been hypothesized to be important sites of plasticity that can be strengthened when a dLGN neuron loses its dominant RGC input[72] or in response to salient environmental features.[73] Further work is needed to understand the complex functions and computations that weak inputs may facilitate.

Limitations of the study

This study employed both *in vivo* and *in vitro* approaches to measure functional connections between RGCs and dLGN neurons. While both approaches directly assess functional connectivity, comparisons between them should be interpreted with caution due to differences in opsins expressed in RGCs, optical stimulation efficiency, axonal viability between preparations, contributions from inhibitory circuits, and dLGN locations sampled. In particular, *in vivo* recordings spanned the entire depth of the dLGN, while *in vitro* slice recordings selectively sampled the ventro-posterior region of dLGN (Figure 6G), making it difficult to directly compare proportions of neurons that receive strong functional inputs. Additionally, *in vitro* recordings were selectively made from TC neurons,[74] whereas *in vivo* recordings include responses from both TC neurons and interneurons, which cannot be distinguished by extracellular spike waveform.[75–77] However, as interneurons constitute roughly 10% of dLGN neurons,[78] the vast majority of *in vivo* recordings likely reflect TC neuron activity.

It is also important to note that in this study, entire populations of RGCs were simultaneously activated using optogenetics, rather than single RGC axons. As a result, we were not able to estimate divergence of single RGC inputs onto dLGN neurons as has been previously done using simultaneous recordings from RGCs and dLGN neurons in cats.[5,7–9,14,15] Moreover, our approach cannot distinguish whether reliably driven cells were innervated by many weak inputs of the same RGC type or whether a single RGC provided a strong input. Despite these limitations, our study shows that principles governing circuit function in the dLGN are remarkably conserved across species. Our results also point to the potential for flexibility in visual processing that can be the focus of future investigation.

RESOURCE AVAILABILITY

Lead contact

Requests for further information or resources should be directed to and will be fulfilled by the lead contact, Chinfei Chen (chinfei.chen@childrens.harvard.edu).

Materials availability

This study did not generate new, unique reagents.

Data and code availability

- All data reported in this paper will be shared by the lead contact upon request.
- This paper does not report original code.
- Any additional information required to reanalyze the data reported in this paper is available from the lead contact upon request.

ACKNOWLEDGMENTS

This work was supported by NIH R01EY013613 to C.C., NIH R01EY035268 to W.W., NIH F32EY033202 to T.S., NIH T32NS007473 to T.S., the Leonard and Isabelle Goldenson Fellowship to T.S., the William Randolph Hearst Fellowship to Q.J., NIH P50HD105351 for the Administrative and Cellular Imaging Cores, NIH P30EY012196 for the Viral Core, and NIH S10OD030322 and NIH S10OD016453 to C.C.

AUTHOR CONTRIBUTIONS

Conceptualization, T.S., Q.J., and C.C.; resources, W.W. and C.C.; formal analysis, T.S., Q.J., I.J.-M., and H.A.L.; investigation, T.S., Q.J., I.J.-M., H.R.,

and H.A.L.; writing – original draft, T.S., Q.J., and C.C.; writing – review & editing, T.S., Q.J., I.J.-M., W.W., and C.C.; visualization, T.S., Q.J., I.J.-M., and H.A.L.; funding acquisition, T.S., Q.J., W.W., and C.C.

DECLARATION OF INTERESTS

The authors declare no competing interests.

STAR★METHODS

Detailed methods are provided in the online version of this paper and include the following:

- KEY RESOURCES TABLE
- EXPERIMENTAL MODEL AND STUDY PARTICIPANT DETAILS
  - Animals
- METHOD DETAILS
  - Intravitreal injection of adeno-associated viruses (AAVs)
  - Perfusion and immunohistochemical staining
  - Confocal microscopy
  - *In vivo* electrophysiology
  - Visual stimuli and optogenetic stimulation *in vivo*
  - *In vitro* slice electrophysiology
  - Dual-opsin stimulation
- QUANTIFICATION AND STATISTICAL ANALYSIS
  - Analysis of *in vivo* electrophysiology data
  - Two-photon calcium imaging of ooDSGCs
  - Quantification of axonal projection patterns in the dLGN
  - Analysis of slice electrophysiology data

SUPPLEMENTAL INFORMATION

Supplemental information can be found online at https://doi.org/10.1016/j.neuron.2025.06.015.

Received: September 7, 2024
Revised: May 8, 2025
Accepted: June 19, 2025
Published: July 21, 2025

REFERENCES

1. Usrey, W.M., and Alitto, H.J. (2015). Visual Functions of the Thalamus. Annu. Rev. Vis. Sci. *1*, 351–371. https://doi.org/10.1146/annurev-vision-082114-035920.
2. Hooks, B.M., and Chen, C. (2020). Circuitry Underlying Experience-Dependent Plasticity in the Mouse Visual System. Neuron *106*, 21–36. https://doi.org/10.1016/j.neuron.2020.01.031.
3. Seabrook, T.A., Burbridge, T.J., Crair, M.C., and Huberman, A.D. (2017). Architecture, Function, and Assembly of the Mouse Visual System. Annu. Rev. Neurosci. *40*, 499–538. https://doi.org/10.1146/annurev-neuro-071714-033842.
4. Liang, L., and Chen, C. (2020). Organization, Function, and Development of the Mouse Retinogeniculate Synapse. Annu. Rev. Vis. Sci. *6*, 261–285. https://doi.org/10.1146/annurev-vision-121219-081753.
5. Hubel, D.H., and Wiesel, T.N. (1961). Integrative action in the cat's lateral geniculate body. J. Physiol. *155*, 385–398. https://doi.org/10.1113/jphysiol.1961.sp006635.
6. Bishop, P.O., Burke, W., and Davis, R. (1958). Synapse Discharge by Single Fibre in Mammalian Visual System. Nature *182*, 728–730. https://doi.org/10.1038/182728b0.
7. Cleland, B.G., Dubin, M.W., and Levick, W.R. (1971). Simultaneous Recording of Input and Output of Lateral Geniculate Neurones. Nat. New Biol. *231*, 191–192. https://doi.org/10.1038/newbio231191a0.
8. Usrey, W.M., Reppas, J.B., and Reid, R.C. (1999). Specificity and Strength of Retinogeniculate Connections. J. Neurophysiol. *82*, 3527–3540. https://doi.org/10.1152/jn.1999.82.6.3527.
9. Usrey, W.M., Reppas, J.B., and Reid, R.C. (1998). Paired-spike interactions and synaptic efficacy of retinal inputs to the thalamus. Nature *395*, 384–387. https://doi.org/10.1038/26487.
10. Mastronarde, D.N. (1992). Nonlagged relay cells and interneurons in the cat lateral geniculate nucleus: receptive-field properties and retinal inputs. Vis. Neurosci. *8*, 407–441. https://doi.org/10.1017/s0952523800004934.
11. Cleland, B.G., Dubin, M.W., and Levick, W.R. (1971). Sustained and transient neurones in the cat's retina and lateral geniculate nucleus. J. Physiol. *217*, 473–496. https://doi.org/10.1113/jphysiol.1971.sp009581.
12. Mastronarde, D.N. (1987). Two classes of single-input X-cells in cat lateral geniculate nucleus. I. Receptive-field properties and classification of cells. J. Neurophysiol. *57*, 357–380. https://doi.org/10.1152/jn.1987.57.2.357.
13. Bauer, J., Weiler, S., Fernholz, M.H.P., Laubender, D., Scheuss, V., Hübener, M., Bonhoeffer, T., and Rose, T. (2021). Limited functional convergence of eye-specific inputs in the retinogeniculate pathway of the mouse. Neuron *109*, 2457–2468.e12. https://doi.org/10.1016/j.neuron.2021.05.036.
14. Yeh, C.-I., Stoelzel, C.R., Weng, C., and Alonso, J.-M. (2009). Functional Consequences of Neuronal Divergence Within the Retinogeniculate Pathway. J. Neurophysiol. *101*, 2166–2185. https://doi.org/10.1152/jn.91088.2008.
15. Alonso, J.M., Usrey, W.M., and Reid, R.C. (1996). Precisely correlated firing in cells of the lateral geniculate nucleus. Nature *383*, 815–819. https://doi.org/10.1038/383815a0.
16. Hammer, S., Monavarfeshani, A., Lemon, T., Su, J., and Fox, M.A. (2015). Multiple Retinal Axons Converge onto Relay Cells in the Adult Mouse Thalamus. Cell Rep. *12*, 1575–1583. https://doi.org/10.1016/j.celrep.2015.08.003.
17. Litvina, E.Y., and Chen, C. (2017). Functional Convergence at the Retinogeniculate Synapse. Neuron *96*, 330–338.e5. https://doi.org/10.1016/j.neuron.2017.09.037.
18. Morgan, J.L., Berger, D.R., Wetzel, A.W., and Lichtman, J.W. (2016). The Fuzzy Logic of Network Connectivity in Mouse Visual Thalamus. Cell *165*, 192–206. https://doi.org/10.1016/j.cell.2016.02.033.
19. Rompani, S.B., Müllner, F.E., Wanner, A., Zhang, C., Roth, C.N., Yonehara, K., and Roska, B. (2017). Different Modes of Visual Integration in the Lateral Geniculate Nucleus Revealed by Single-Cell-Initiated Transsynaptic Tracing. Neuron *93*, 767–776.e6. https://doi.org/10.1016/j.neuron.2017.01.028.
20. Jiang, Q., Litvina, E.Y., Acarón Ledesma, H., Shu, G., Sonoda, T., Wei, W., and Chen, C. (2022). Functional convergence of on-off direction-selective ganglion cells in the visual thalamus. Curr. Biol. *32*, 3110–3120.e6. https://doi.org/10.1016/j.cub.2022.06.023.
21. Liang, L., Fratzl, A., Goldey, G., Ramesh, R.N., Sugden, A.U., Morgan, J.L., Chen, C., and Andermann, M.L. (2018). A Fine-Scale Functional Logic to Convergence from Retina to Thalamus. Cell *173*, 1343–1355.e24. https://doi.org/10.1016/j.cell.2018.04.041.
22. Kerschensteiner, D. (2022). Feature Detection by Retinal Ganglion Cells. Annu. Rev. Vis. Sci. *8*, 135–169. https://doi.org/10.1146/annurev-vision-100419-112009.
23. Nassi, J.J., and Callaway, E.M. (2009). Parallel processing strategies of the primate visual system. Nat. Rev. Neurosci. *10*, 360–372. https://doi.org/10.1038/nrn2619.
24. Suresh, V., Çiftçioğlu, U.M., Wang, X., Lala, B.M., Ding, K.R., Smith, W.A., Sommer, F.T., and Hirsch, J.A. (2016). Synaptic Contributions to Receptive Field Structure and Response Properties in the Rodent Lateral Geniculate Nucleus of the Thalamus. J. Neurosci. *36*, 10949–10963. https://doi.org/10.1523/JNEUROSCI.1045-16.2016.
25. Sincich, L.C., Adams, D.L., Economides, J.R., and Horton, J.C. (2007). Transmission of Spike Trains at the Retinogeniculate Synapse.

J. Neurosci. *27*, 2683–2692. https://doi.org/10.1523/JNEUROSCI.5077-06.2007.

26. Wang, X., Wei, Y., Vaingankar, V., Wang, Q., Koepsell, K., Sommer, F.T., and Hirsch, J.A. (2007). Feedforward Excitation and Inhibition Evoke Dual Modes of Firing in the Cat's Visual Thalamus during Naturalistic Viewing. Neuron *55*, 465–478. https://doi.org/10.1016/j.neuron.2007.06.039.
27. Rowan, S., and Cepko, C.L. (2004). Genetic analysis of the homeodomain transcription factor Chx10 in the retina using a novel multifunctional BAC transgenic mouse reporter. Dev. Biol. *271*, 388–402. https://doi.org/10.1016/j.ydbio.2004.03.039.
28. Piscopo, D.M., El-Danaf, R.N., Huberman, A.D., and Niell, C.M. (2013). Diverse Visual Features Encoded in Mouse Lateral Geniculate Nucleus. J. Neurosci. *33*, 4642–4656. https://doi.org/10.1523/JNEUROSCI.5187-12.2013.
29. Zhao, X., Chen, H., Liu, X., and Cang, J. (2013). Orientation-selective Responses in the Mouse Lateral Geniculate Nucleus. J. Neurosci. *33*, 12751–12763. https://doi.org/10.1523/JNEUROSCI.0095-13.2013.
30. Scholl, B., Tan, A.Y.Y., Corey, J., and Priebe, N.J. (2013). Emergence of Orientation Selectivity in the Mammalian Visual Pathway. J. Neurosci. *33*, 10616–10624. https://doi.org/10.1523/JNEUROSCI.0404-13.2013.
31. Summers, M.T., and Feller, M.B. (2022). Distinct inhibitory pathways control velocity and directional tuning in the mouse retina. Curr. Biol. *32*, 2130–2143.e3. https://doi.org/10.1016/j.cub.2022.03.054.
32. Wei, W. (2018). Neural Mechanisms of Motion Processing in the Mammalian Retina. Annu. Rev. Vis. Sci. *4*, 165–192. https://doi.org/10.1146/annurev-vision-091517-034048.
33. Duan, X., Krishnaswamy, A., De la Huerta, I., and Sanes, J.R. (2014). Type II Cadherins Guide Assembly of a Direction-Selective Retinal Circuit. Cell *158*, 793–807. https://doi.org/10.1016/j.cell.2014.06.047.
34. Duan, X., Qiao, M., Bei, F., Kim, I.-J., He, Z., and Sanes, J.R. (2015). Subtype-Specific Regeneration of Retinal Ganglion Cells following Axotomy: Effects of Osteopontin and mTOR Signaling. Neuron *85*, 1244–1256. https://doi.org/10.1016/j.neuron.2015.02.017.
35. Krieger, B., Qiao, M., Rousso, D.L., Sanes, J.R., and Meister, M. (2017). Four alpha ganglion cell types in mouse retina: Function, structure, and molecular signatures. PLOS One *12*, e0180091. https://doi.org/10.1371/journal.pone.0180091.
36. Bedbrook, C.N., Yang, K.K., Robinson, J.E., Mackey, E.D., Gradinaru, V., and Arnold, F.H. (2019). Machine learning-guided channelrhodopsin engineering enables minimally invasive optogenetics. Nat. Methods *16*, 1176–1184. https://doi.org/10.1038/s41592-019-0583-8.
37. Pang, J.-J., Gao, F., and Wu, S.M. (2003). Light-Evoked Excitatory and Inhibitory Synaptic Inputs to ON and OFF α Ganglion Cells in the Mouse Retina. J. Neurosci. *23*, 6063–6073. https://doi.org/10.1523/JNEUROSCI.23-14-06063.2003.
38. Estevez, M.E., Fogerson, P.M., Ilardi, M.C., Borghuis, B.G., Chan, E., Weng, S., Auferkorte, O.N., Demb, J.B., and Berson, D.M. (2012). Form and Function of the M4 Cell, an Intrinsically Photosensitive Retinal Ganglion Cell Type Contributing to Geniculocortical Vision. J. Neurosci. *32*, 13608–13620. https://doi.org/10.1523/JNEUROSCI.1422-12.2012.
39. Klapoetke, N.C., Murata, Y., Kim, S.S., Pulver, S.R., Birdsey-Benson, A., Cho, Y.K., Morimoto, T.K., Chuong, A.S., Carpenter, E.J., Tian, Z., et al. (2014). Independent optical excitation of distinct neural populations. Nat. Methods *11*, 338–346. https://doi.org/10.1038/nmeth.2836.
40. Kleinlogel, S., Feldbauer, K., Dempski, R.E., Fotis, H., Wood, P.G., Bamann, C., and Bamberg, E. (2011). Ultra light-sensitive and fast neuronal activation with the Ca2+-permeable channelrhodopsin CatCh. Nat. Neurosci. *14*, 513–518. https://doi.org/10.1038/nn.2776.
41. Jüttner, J., Szabo, A., Gross-Scherf, B., Morikawa, R.K., Rompani, S.B., Hantz, P., Szikra, T., Esposti, F., Cowan, C.S., Bharioke, A., et al. (2019). Targeting neuronal and glial cell types with synthetic promoter AAVs in mice, non-human primates and humans. Nat. Neurosci. *22*, 1345–1356. https://doi.org/10.1038/s41593-019-0431-2.
42. Kay, J.N., De la Huerta, I., Kim, I.-J., Zhang, Y., Yamagata, M., Chu, M.W., Meister, M., and Sanes, J.R. (2011). Retinal Ganglion Cells with Distinct Directional Preferences Differ in Molecular Identity, Structure, and Central Projections. J. Neurosci. *31*, 7753–7762. https://doi.org/10.1523/JNEUROSCI.0907-11.2011.
43. Sabbah, S., Gemmer, J.A., Bhatia-Lin, A., Manoff, G., Castro, G., Siegel, J.K., Jeffery, N., and Berson, D.M. (2017). A retinal code for motion along the gravitational and body axes. Nature *546*, 492–497. https://doi.org/10.1038/nature22818.
44. Cruz-Martín, A., El-Danaf, R.N., Osakada, F., Sriram, B., Dhande, O.S., Nguyen, P.L., Callaway, E.M., Ghosh, A., and Huberman, A.D. (2014). A dedicated circuit links direction-selective retinal ganglion cells to the primary visual cortex. Nature *507*, 358–361. https://doi.org/10.1038/nature12989.
45. Martersteck, E.M., Hirokawa, K.E., Evarts, M., Bernard, A., Duan, X., Li, Y., Ng, L., Oh, S.W., Ouellette, B., Royall, J.J., et al. (2017). Diverse Central Projection Patterns of Retinal Ganglion Cells. Cell Rep. *18*, 2058–2072. https://doi.org/10.1016/j.celrep.2017.01.075.
46. Bickford, M.E., Zhou, N., Krahe, T.E., Govindaiah, G., and Guido, W. (2015). Retinal and Tectal "Driver-Like" Inputs Converge in the Shell of the Mouse Dorsal Lateral Geniculate Nucleus. J. Neurosci. *35*, 10523–10534. https://doi.org/10.1523/JNEUROSCI.3375-14.2015.
47. Turner, J.P., and Salt, T.E. (1998). Characterization of sensory and corticothalamic excitatory inputs to rat thalamocortical neurones in vitro. J. Physiol. *510*, 829–843. https://doi.org/10.1111/j.1469-7793.1998.829bj.x.
48. Hooks, B.M., Lin, J.Y., Guo, C., and Svoboda, K. (2015). Dual-Channel Circuit Mapping Reveals Sensorimotor Convergence in the Primary Motor Cortex. J. Neurosci. *35*, 4418–4426. https://doi.org/10.1523/JNEUROSCI.3741-14.2015.
49. Hooks, B.M., and Chen, C. (2006). Distinct Roles for Spontaneous and Visual Activity in Remodeling of the Retinogeniculate Synapse. Neuron *52*, 281–291. https://doi.org/10.1016/j.neuron.2006.07.007.
50. Chen, C., and Regehr, W.G. (2000). Developmental Remodeling of the Retinogeniculate Synapse. Neuron *28*, 955–966. https://doi.org/10.1016/s0896-6273(00)00166-5.
51. Liu, X., and Chen, C. (2008). Different Roles for AMPA and NMDA Receptors in Transmission at the Immature Retinogeniculate Synapse. J. Neurophysiol. *99*, 629–643. https://doi.org/10.1152/jn.01171.2007.
52. McCormick, D.A., Nestvogel, D.B., and He, B.J. (2020). Neuromodulation of Brain State and Behavior. Annu. Rev. Neurosci. *43*, 391–415. https://doi.org/10.1146/annurev-neuro-100219-105424.
53. Román Rosón, M., Bauer, Y., Kotkat, A.H., Berens, P., Euler, T., and Busse, L. (2019). Mouse dLGN Receives Functional Input from a Diverse Population of Retinal Ganglion Cells with Limited Convergence. Neuron *102*, 462–476.e8. https://doi.org/10.1016/j.neuron.2019.01.040.
54. Sun, W., Tan, Z., Mensh, B.D., and Ji, N. (2016). Thalamus provides layer 4 of primary visual cortex with orientation- and direction-tuned inputs. Nat. Neurosci. *19*, 308–315. https://doi.org/10.1038/nn.4196.
55. Wang, H., Dey, O., Lagos, W.N., Behnam, N., Callaway, E.M., and Stafford, B.K. (2024). Parallel pathways carrying direction-and orientation-selective retinal signals to layer 4 of the mouse visual cortex. Cell Rep. *43*, 113830. https://doi.org/10.1016/j.celrep.2024.113830.
56. Bereshpolova, Y., Stoelzel, C.R., Su, C., Alonso, J.-M., and Swadlow, H.A. (2019). Activation of a Visual Cortical Column by a Directionally Selective Thalamocortical Neuron. Cell Rep. *27*, 3733–3740.e3. https://doi.org/10.1016/j.celrep.2019.05.094.
57. Su, C., Mendes-Platt, R.F., Alonso, J.-M., Swadlow, H.A., and Bereshpolova, Y. (2025). Retinal direction of motion is reliably transmitted to visual cortex through highly selective thalamocortical connections. Curr. Biol. *35*, 217–223.e4. https://doi.org/10.1016/j.cub.2024.11.013.

58. Rousso, D.L., Qiao, M., Kagan, R.D., Yamagata, M., Palmiter, R.D., and Sanes, J.R. (2016). Two Pairs of ON and OFF Retinal Ganglion Cells Are Defined by Intersectional Patterns of Transcription Factor Expression. Cell Rep. *15*, 1930–1944. https://doi.org/10.1016/j.celrep.2016.04.069.

59. Sivyer, B., Tomlinson, A., and Taylor, W.R. (2019). Simulated Saccadic Stimuli Suppress ON-Type Direction-Selective Retinal Ganglion Cells via Glycinergic Inhibition. J. Neurosci. *39*, 4312–4322. https://doi.org/10.1523/JNEUROSCI.3066-18.2019.

60. Mani, A., Yang, X., Zhao, T.A., Leyrer, M.L., Schreck, D., and Berson, D.M. (2023). A circuit suppressing retinal drive to the optokinetic system during fast image motion. Nat. Commun. *14*, 5142. https://doi.org/10.1038/s41467-023-40527-z.

61. Hillier, D., Fiscella, M., Drinnenberg, A., Trenholm, S., Rompani, S.B., Raics, Z., Katona, G., Juettner, J., Hierlemann, A., Rozsa, B., et al. (2017). Causal evidence for retina-dependent and -independent visual motion computations in mouse cortex. Nat. Neurosci. *20*, 960–968. https://doi.org/10.1038/nn.4566.

62. Reggiani, J.D.S., Jiang, Q., Barbini, M., Lutas, A., Liang, L., Fernando, J., Deng, F., Wan, J., Li, Y., Chen, C., et al. (2023). Brainstem serotonin neurons selectively gate retinal information flow to thalamus. Neuron *111*, 711–726.e11. https://doi.org/10.1016/j.neuron.2022.12.006.

63. Liang, L., Fratzl, A., Reggiani, J.D.S., El Mansour, O.E., Chen, C., and Andermann, M.L. (2020). Retinal Inputs to the Thalamus Are Selectively Gated by Arousal. Curr. Biol. *30*, 3923–3934.e9. https://doi.org/10.1016/j.cub.2020.07.065.

64. Monckton, J.E., and McCormick, D.A. (2002). Neuromodulatory Role of Serotonin in the Ferret Thalamus. J. Neurophysiol. *87*, 2124–2136. https://doi.org/10.1152/jn.00650.2001.

65. Erisken, S., Vaiceliunaite, A., Jurjut, O., Fiorini, M., Katzner, S., and Busse, L. (2014). Effects of Locomotion Extend throughout the Mouse Early Visual System. Curr. Biol. *24*, 2899–2907. https://doi.org/10.1016/j.cub.2014.10.045.

66. Peelman, K., and Haider, B. (2025). Environmental context influences visual processing in thalamus. Curr. Biol. *35*, 1422–1430.e5. https://doi.org/10.1016/j.cub.2025.02.009.

67. Socha, K.Z., Couto, J., Whiteway, M.R., Hosseinjany, S., Butts, D.A., and Bonin, V. (2024). Behavioral modulations can alter the visual tuning of neurons in the mouse thalamocortical pathway. Cell Rep. *43*, 114947. https://doi.org/10.1016/j.celrep.2024.114947.

68. Xiaojuan, H. (黑晓娟), Stoelzel, C.R., jun, Z. (庄骏), Bereshpolova, Y., Huff, J. M., Alonso, J.-M., and Swadlow, H.A. (2014). Directional selective neurons in the awake LGN: response properties and modulation by brain state. J. Neurophysiol. *112*, 362–373. https://doi.org/10.1152/jn.00121.2014.

69. Hamos, J.E., Van Horn, S.C., Raczkowski, D., and Sherman, S.M. (1987). Synaptic circuits involving an individual retinogeniculate axon in the cat. J. Comp. Neurol. *259*, 165–192. https://doi.org/10.1002/cne.902590202.

70. Martinez, L.M., Molano-Mazón, M., Wang, X., Sommer, F.T., and Hirsch, J.A. (2014). Statistical Wiring of Thalamic Receptive Fields Optimizes Spatial Sampling of the Retinal Image. Neuron *81*, 943–956. https://doi.org/10.1016/j.neuron.2013.12.014.

71. Alonso, J.M., Yeh, C.I., Weng, C., and Stoelzel, C. (2006). Retinogeniculate connections: a balancing act between connection specificity and receptive field diversity. Prog. Brain Res. *154*, 3–13. https://doi.org/10.1016/S0079-6123(06)54001-4.

72. Moore, B.D., Kiley, C.W., Sun, C., and Usrey, W.M. (2011). Rapid Plasticity of Visual Responses in the Adult Lateral Geniculate Nucleus. Neuron *71*, 812–819. https://doi.org/10.1016/j.neuron.2011.06.025.

73. Sonoda, T., Stephany, C.-É., Kelley, K., Kang, D., Wu, R., Uzgare, M.R., Fagiolini, M., Greenberg, M.E., and Chen, C. (2025). Experience influences the refinement of feature selectivity in the mouse primary visual thalamus. Neuron *113*, 1352–1362.e4. https://doi.org/10.1016/j.neuron.2025.02.023.

74. Sherman, S.M. (2004). Interneurons and triadic circuitry of the thalamus. Trends Neurosci. *27*, 670–675. https://doi.org/10.1016/j.tins.2004.08.003.

75. Pape, H.C., and McCormick, D.A. (1995). Electrophysiological and pharmacological properties of interneurons in the cat dorsal lateral geniculate nucleus. Neuroscience *68*, 1105–1125. https://doi.org/10.1016/0306-4522(95)00205-w.

76. Gorin, A.S., Miao, Y., Ahn, S., Suresh, V., Su, Y., Ciftcioglu, U.M., Sommer, F.T., and Hirsch, J.A. (2023). Local interneurons in the murine visual thalamus have diverse receptive fields and can provide feature selective inhibition to relay cells. Preprint at bioRxiv. https://doi.org/10.1101/2023.08.10.549394.

77. Wang, X., Vaingankar, V., Soto Sanchez, C., Sommer, F.T., and Hirsch, J. A. (2011). Thalamic interneurons and relay cells use complementary synaptic mechanisms for visual processing. Nat. Neurosci. *14*, 224–231. https://doi.org/10.1038/nn.2707.

78. Evangelio, M., García-Amado, M., and Clascá, F. (2018). Thalamocortical Projection Neuron and Interneuron Numbers in the Visual Thalamic Nuclei of the Adult C57BL/6 Mouse. Front. Neuroanat. *12*, 27. https://doi.org/10.3389/fnana.2018.00027.

79. Pachitariu, M., Sridhar, S., and Stringer, C. (2023). Solving the spike sorting problem with Kilosort. Preprint at bioRxiv. https://doi.org/10.1101/2023.01.07.523036.

80. Brainard, D.H. (1997). The Psychophysics Toolbox. Spat. Vis. *10*, 433–436. https://doi.org/10.1163/156856897x00357.

81. Madisen, L., Mao, T., Koch, H., Zhuo, J.M., Berenyi, A., Fujisawa, S., Hsu, Y.-W.A., Garcia, A.J., Gu, X., Zanella, S., et al. (2012). A toolbox of Cre-dependent optogenetic transgenic mice for light-induced activation and silencing. Nat. Neurosci. *15*, 793–802. https://doi.org/10.1038/nn.3078.

82. Durand, S., Iyer, R., Mizuseki, K., de Vries, S., Mihalas, S., and Reid, R.C. (2016). A Comparison of Visual Response Properties in the Lateral Geniculate Nucleus and Primary Visual Cortex of Awake and Anesthetized Mice. J. Neurosci. *36*, 12144–12156. https://doi.org/10.1523/JNEUROSCI.1741-16.2016.

83. Pressler, R.T., and Regehr, W.G. (2013). Metabotropic Glutamate Receptors Drive Global Persistent Inhibition in the Visual Thalamus. J. Neurosci. *33*, 2494–2506. https://doi.org/10.1523/JNEUROSCI.3458-12.2013.

84. Hauser, J.L., Edson, E.B., Hooks, B.M., and Chen, C. (2013). Metabotropic glutamate receptors and glutamate transporters shape transmission at the developing retinogeniculate synapse. J. Neurophysiol. *109*, 113–123. https://doi.org/10.1152/jn.00897.2012.

85. Hauser, J.L., Liu, X., Litvina, E.Y., and Chen, C. (2014). Prolonged synaptic currents increase relay neuron firing at the developing retinogeniculate synapse. J. Neurophysiol. *112*, 1714–1728. https://doi.org/10.1152/jn.00451.2014.

86. Yang, Y.C., Hu, C.C., Huang, C.S., and Chou, P.Y. (2014). Thalamic synaptic transmission of sensory information modulated by synergistic interaction of adenosine and serotonin. J. Neurochem. *128*, 852–863. https://doi.org/10.1111/jnc.12499.

87. Kingston, A.E., Ornstein, P.L., Wright, R.A., Johnson, B.G., Mayne, N.G., Burnett, J.P., Belagaje, R., Wu, S., and Schoepp, D.D. (1998). LY341495 is a nanomolar potent and selective antagonist of group II metabotropic glutamate receptors. Neuropharmacology *37*, 1–12. https://doi.org/10.1016/s0028-3908(97)00191-3.

88. Chen, C., and Regehr, W.G. (2003). Presynaptic Modulation of the Retinogeniculate Synapse. J. Neurosci. *23*, 3130–3135. https://doi.org/10.1523/JNEUROSCI.23-08-03130.2003.

89. Baden, T., Berens, P., Franke, K., Román Rosón, M., Bethge, M., and Euler, T. (2016). The functional diversity of retinal ganglion cells in the mouse. Nature *529*, 345–350. https://doi.org/10.1038/nature16468.

STAR★METHODS

KEY RESOURCES TABLE

REAGENT or RESOURCE	SOURCE	IDENTIFIER
Antibodies		
Chicken anti-GFP	Abcam	Cat# ab13970; RRID: AB_300798
Rabbit anti-RFP	Rockland	Cat# 600-401-379; RRID: AB_2209751
Rabbit anti-CART	Phoenix Pharmaceuticals	Cat# H-003-62; RRID: AB_2313614
Goat anti-chicken IgY (H+L) (Alexa Fluor 488)	Invitrogen	Cat# A11039; RRID: AB_2534096
Goat anti-rabbit IgG (H+L) (Alexa Fluor Plus 555)	Invitrogen	Cat# A32732; RRID: AB_2633281
Bacterial and virus strains		
AAV2/7m8-CAG-DIO-ChRger2-YFP	BCH Viral Core	N/A
AAV2/7m8-hSyn-DIO-ChrimsonR-tdTomato	BCH Viral Core	N/A
AAV2/7m8-ProD1-CatCh-GFP	BCH Viral Core	N/A
Chemicals, peptides, and recombinant proteins		
DiI	Invitrogen	Cat# V22885
Alexa Fluor 647 Hydrazide	Thermo Fisher	Cat# A20502
(+)-Bicuculline	Tocris	Cat# 0130
CGP 55845 hydrochloride	Tocris	Cat# 1248
DPCPX	Tocris	Cat# 0439
LY341495	Tocris	Cat# 1209
Experimental models: Organisms/strains		
Mouse: Chx10-Cre	The Jackson Laboratory	Cat# 005105; RRID: IMSR_JAX:005105
Mouse: Cart-IRES2-Cre-D	The Jackson Laboratory	Cat# 028533; RRID: IMSR_JAX:028533
Mouse: Ai32	The Jackson Laboratory	Cat# 012569; RRID: IMSR_JAX:012569
Mouse: Kcng4-Cre	The Jackson Laboratory	Cat# 029414; RRID: IMSR_JAX:029414
Mouse: Ai95D	The Jackson Laboratory	Cat# 028865; RRID: IMSR_JAX:028865
Recombinant DNA		
pAAV-CAG-DIO(ChRger2-TS-YFP)	Addgene	Cat# 127239; RRID: Addgene_127239
pAAV-Syn-FLEX-rc[ChrimsonR-tdTomato]	Addgene	Cat# 62723; RRID: Addgene_62723
198_pAAV-ProD1-CatCh-GFP-WPRE	Addgene	Cat# 125977; RRID: Addgene_125977
Software and algorithms		
MATLAB 2019b	MathWorks	https://www.mathworks.com/products/matlab.html; RRID: SCR_001622
ImageJ (Fiji)	NIH – public domain	https://imagej.net/Fiji; RRID: SCR_002285
Prism 8	Graphpad	https://www.graphpad.com/ scientific-software/prism/; RRID: SCR_005375
Kilosort2	Pachitariu et al.[79]	RRID: SCR_016422
Psychophysics Toolbox	Brainard[80]	RRID: SCR_002881
Synapse	Tucker-Davis Technologies	https://www.tdt.com/component/synapse-software/
Igor Pro	WaveMetrics	https://www.wavemetrics.com/products/igorpro; RRID: SCR_000325
Other		
32-channel silicon probe	Cambridge Neurotech	Cat#: ASSY-37-H7b
32-channel silicon probe	NeuroNexus	Cat#: A1x32-5mm-25-177
Nanoject III	Drummond Scientific	Cat#: 3-000-207

EXPERIMENTAL MODEL AND STUDY PARTICIPANT DETAILS

Animals

All procedures complied with the NIH Guide for the Care and Use of Laboratory Animals and were approved by the Institutional Animal Care and Use Committee (IACUC) at Boston Children's Hospital. Both male and female mice were used, all on a C57 BL/6J background (Jackson Laboratories strain #000664). To express channelrhodopsin-2 (ChR2) in all RGCs, *Chx10-Cre* (JAX Strain #005105)[17,27] mice were crossed to *Ai32* (JAX Strain #012569).[81] To express ChR2 in on-off direction selective RGCs (ooDSGCs) for *in vivo* recording experiments, *Cart-IRES2-Cre-D* (JAX Strain #028533) mice were crossed to *Ai32* mice. To detect the tuning properties of ooDSGCs in the retina, *Cart-IRES2-Cre-D* mice were crossed to *Ai95D* floxed GCaMP6f mice (JAX Strain #028865). For labeling and activating α-RGCs, *Kcng4-Cre* (JAX Strain #029414)[33] mice were used for both *in vivo* and dual-opsin slice recordings with intravitreal injection of adeno-associated viruses (see below).

METHOD DETAILS

Intravitreal injection of adeno-associated viruses (AAVs)

Intravitreal injections of AAVs were performed in *Kcng4-Cre* mice for both *in vivo* electrophysiology (Figure 5) and dual-opsin *in vitro* slice experiments (Figures 6, 7, and 8). Mice were initially anesthetized in an isoflurane chamber (3.5% in oxygen) and isoflurane levels were typically maintained at ~1.5% isoflurane in oxygen delivered through a nose cone. For *in vivo* recording experiments, the left eye was injected with 800 nL–1 μL of AAV2/7m8-CAG-DIO-ChRger2-YFP (1.38 x 10^{13} viral particles/mL, Addgene Plasmid #127239 packaged by BCH viral core). For dual-opsin experiments, the left eye was injected with 1 μL of a 1:1 mixture of AAV2/7m8-hSyn-DIO-ChrimsonR-tdTomato (2.96 x 10^{13} viral particles/mL, Addgene Plasmid #62723 packaged by BCH viral core) and AAV2/7m8-ProD1-CatCh-GFP (2.25 x 10^{13} viral particles/mL, Addgene Plasmid #125977 packaged by BCH viral core). Injections were made with a sharp glass pipette attached to either a 10 μL Hamilton syringe or a Nanoject III microinjector (Drummond Scientific). Intravitreal injections were performed between postnatal day 20 (P20) and P30. Following virus injection, *Kcng4-Cre* mice were housed under a standard 12:12 light dark cycle until experiments were performed between P50 and P100.

Perfusion and immunohistochemical staining

For sampling of retinas or brain tissues to detect the expression of ChrimsonR-tdTomato and CatCh-GFP for dual-opsin experiments, mice were euthanized with 10% pentobarbital and transcardially perfused with 0.1 M phosphate buffered saline (PBS) immediately followed by 4% w/v paraformaldehyde (PFA) in PBS. Eyes were removed and post-fixed in 4% PFA for 1 h. Retinas were then dissected and rinsed in PBS before immunostaining. Brains were post-fixed overnight in 4% PFA at 4°C and rinsed in PBS. Brain slices containing dLGN were coronally sectioned on a Leica VT1000 vibratome with a thickness of 60 μm. Following *in vitro* electrophysiological experiments, parasagittal brain slices (250 μm) were collected, incubated in 4% PFA for 1 h, and kept in PBS until immunostaining.

For whole-mount retina staining, retinas were blocked in PBS containing 5% normal goat serum (NGS) and 0.1% Triton X-100 at room temperature for 1 h. Then primary antibodies were applied in PBS containing 0.3% Triton and 2% NGS: chicken anti-GFP (1:1000; ab13970, Abcam), rabbit anti-RFP (1:1000; 600-401-379, Rockland) or rabbit anti-CART (1:1000; H-003-62, Phoenix Pharmaceuticals), at 4°C for 2-3 days. After rinsing with 0.1% Triton/PBS, retinas were incubated with secondary antibodies at 4°C for another 2-3 days: goat anti-chicken antibody conjugated to Alexa Fluor 488 (1:1000; A11039, Invitrogen), goat anti-rabbit 555 (1:1000; A32732, Invitrogen) or goat anti-rabbit 647 (1:1000; A21245, Invitrogen). Retinas were then mounted and cover-slipped with Vectashield (H-1000, VectorLabs).

Coronal brain slices containing dLGN were stained with GFP and RFP overnight to label the axonal terminals from the dual-opsin-labeled RGCs, followed by secondary antibody incubation for 2 h at room temperature. In electrophysiological experiments, patched cells were filled with Alexa Fluor 647 Hydrazide (1 mg/mL; A20502, Thermo Fisher). These parasagittal slices after patching were collected, stained with GFP and RFP following similar procedures to coronal brain slice staining, except that the incubation of primary and secondary antibodies was conducted at 4°C for 2-3 days each.

Confocal microscopy

Whole-mount retina images were taken using Zeiss Axio Imager.Z2 epifluorescence microscope or Leica TCS SP8 Laser Scanning Confocal. To detect the expression of dual opsins in the retina of recorded mice, total numbers of GFP- and RFP-stained RGCs were counted from each retina manually using ImageJ. To quantify the colocalization of Kcng4-Cre$^+$ and ProD1$^+$ RGCs, or CART-IR and ProD1$^+$ RGCs, images of the retina (12 fields of view from each mouse) were acquired through Zeiss LSM710 Multiphoton Confocal using a 20x Olympus objective to detect GFP, RFP or CART signals. Quantification was performed manually using ImageJ. Z-stack and tile scan imaging of the whole dLGN was performed using a Zeiss LSM980 Confocal with a 10x objective. To examine potential convergence of Kcng4-Cre$^+$ and ProD1$^+$ boutons and their interaction with filled postsynaptic neurons in the dLGN, higher resolution Z-stacks were taken under a 63x objective. Volumetric reconstructions of TC neurons, Kcng4-Cre$^+$, and ProD1$^+$ terminals were generated using the "surface" function in Imaris 10.1.1 (Bitplane). To visualize the interaction between the retinal inputs and postsynaptic dendrites, the "surface" of retinal terminals was filtered based on the distance to the TC dendrites (Shortest Distance to

Surfaces = 0) to generate new reconstructions of the three components (Figure S6). The total area of contacts with the TC neuron was measured by using "Surface-Surface Contact Area" tool between the channels of TC neuron and Kcng4-Cre$^+$ terminals, or between the channels of TC neuron and ProD1$^+$ terminals.

In vivo electrophysiology

Surgeries were performed in animals anesthetized with isoflurane (4% for induction and 2% for maintenance). Previous studies have shown that anesthesia does not substantially alter axis- and direction-selectivity in the mouse dLGN, therefore we opted to perform recordings in anesthetized animals for recording stability.[29,82] 2.5 mg/kg dexamethasone was injected subcutaneously to prevent edema and eyes were lubricated with silicone oil to prevent drying. A 2-3 mm diameter craniotomy was performed and was centered ~1.5 mm anterior and ~2.5 mm lateral from the lambda suture. The dLGN was targeted using stereotaxic coordinates 0.7 - 1.4 mm anterior and 2.10 - 2.45 mm lateral from the lambda suture. Up to 2 penetrations were made per animal and penetrations were spaced at least 0.2 mm apart in cartesian coordinates. Recordings were made from the right dLGN and the ipsilateral eye was covered during recordings.

32-channel silicon probes with an attached optical fiber were advanced slowly (<1 μm/s) until the entire dorsal-ventral limits of dLGN were included within the boundaries of the electrode array. Two probe configurations were used in this study: 1) probes with recording sites arranged in a linear configuration with an attached 50 μm diameter optical fiber (Neuronexus, A1x32-5mm-25-177-OA32LP) and 2) probes with recording sites arranged in a staggered configuration with an attached 0.9 mm tapered fiber (Cambridge Neurotech, ASSY-37-H7b). Data were acquired using a PZ5 digitizer with RZ5P processor with Synapse software running on a Workstation 8 computer (Tucker-Davis Technologies). Signals were sampled at 24414 Hz and filtered between 300 Hz and 5 kHz to isolate single units.

Visual stimuli and optogenetic stimulation *in vivo*

Visual stimuli were displayed on a 21 x 12-inch LED monitor, covering approximately 100° x 70° of the visual field. The screen was positioned 22 cm away from the animal's left eye and was offset at a 45° angle relative to the mouse's anteroposterior axis. The screen had a mean luminance of 20 lux. Visual stimuli were gamma corrected and generated using Psychophysics toolbox[80] in MATLAB (MathWorks).

To classify AS and DS dLGN neurons, full-field drifting sine-wave gratings moving in 8 directions were presented. These gratings consisted of 2 spatial frequencies (0.04 and 0.16 cycles/degree) with a temporal frequency of 2 Hz. Gratings were presented for 2 s with an interstimulus interval of 0.5 s. Unique spatial frequency and direction combinations were presented in pseudorandom order over 12 trials and a blank gray screen condition was included to measure spontaneous activity. Following these trials, a second set of gratings with identical parameters was presented after optogenetic stimulation. 20 trials of 1 s full-field luminance flashes were presented to measure ON-OFF responses.

In vivo optogenetic stimulation was delivered using a fiber-coupled 473 nm DPSS laser (Laserglow). During optogenetic stimulation trials, animals viewed a dark screen while 5 Hz pulse trains (each pulse lasting 1 ms, 8-12 mW) were delivered to activate RGC axons in the dLGN. 50 pulse trains were delivered during each recording session. To minimize confounding effects of ChR2 desensitization,[17,48] there was a 10 s interval between each pulse train.

In vitro slice electrophysiology

Brain slices containing the optic tract (OT) and dLGN were prepared as previously described.[17,20] Briefly, mice were anesthetized using isoflurane and decapitated into oxygenated (95% O_2; 5% CO_2) ice-cold cutting solution (in mM): 130 K-gluconate, 15 KCl, 0.05 EGTA, 20 HEPES, and 25 glucose (pH 7.4 adjusted with NaOH, 310-315 mOsm).[83] The brain was then removed quickly and immersed in the ice-cold cutting solution for 60 s. To obtain slices maintaining continuity of retinogeniculate fiber inputs, parasagittal sections were cut as previously described.[47,50] The brain was cut with a steel razor blade, then sectioned into 250 μm-thick slices in oxygenated, ice-cold cutting solution using a sapphire blade (Delaware Diamond Knives) on a vibratome (VT1200S; Leica). Slices containing the dLGN and OT were allowed to recover at 30°C for 15 min in oxygenated saline solution (in mM): 125 NaCl, 26 $NaHCO_3$, 1.25 NaH_2PO_4, 2.5 KCl, 1.0 $MgCl_2$, 2.0 $CaCl_2$, and 25 glucose (pH 7.4, 310-315 mOsm).

To examine potential convergence of Kcng4-Cre$^+$ and ProD1$^+$ inputs in the dLGN, TC neurons from the ventral-posterior region were sampled for whole-cell patch clamp recording. Recordings were performed using a MultiClamp 700B (Axon Instruments), filtered at 1 kHz, and digitized at 20-50 kHz with an ITC-18 interface (Instrutech). Glass pipettes (Drummond Scientific) were pulled on Sutter P-97 Flaming/Brown micropipette puller (Sutter Instruments) and filled with internal solution containing (in mM): 35 CsF, 100 CsCl, 10 EGTA, 10 HEPES, and L-type calcium channel antagonist 0.1 methoxyverapamil (pH 7.3, 290-300 mOsm). The pipette resistance was between 1.5 and 2.0 MOhm. To isolate excitatory synaptic currents, cells were recorded at room temperature in saline solution containing 20 μM of bicuculline ($GABA_A$R antagonist; 0130, Tocris), 2 μM of CGP55845 ($GABA_B$R blocker; 1248, Tocris), 10 μM of DPCPX (antagonist of A1 adenosine receptors; 0439, Tocris), and 50 μM of LY341495 (blocker of presynaptic group II mGluRs; 1209, Tocris),[50,84–87] to block inhibitory circuits and presynaptic neurotransmitter receptors that modulate retinogeniculate release.[50,88] The data acquisition and offline analysis were performed using custom software in IgorPro 8 (Wave-Metrics). Recordings were excluded if access resistance was larger than 10 MOhm or if access resistance changed by more than 20% during a recording.

Dual-opsin stimulation

To obtain the responses to two distinct RGC populations (Kcng4-Cre^{+} and ProD1^{+} RGCs) expressing different opsins, ChrimsonR and CatCh, different wavelengths of light (blue and orange light) were applied to evoke the excitatory postsynaptic currents (oEPSCs) in TC neurons. The blue light (peak at 470 nm, 83 mW/mm^2) and orange light (a wide band ranging between 500 and 700 nm with a high-pass cutoff at 600 nm, 102.4 mW/mm^2) were supplied by a CoolLED pE-300^{ultra} unit through a 60x objective (Olympus LUMplanFL N 60x/1.00W). As an average 20% of light intensity can induce maximal oEPSCs, 100% of light intensity was used to saturate the responses to ensure maximal oEPSCs for both inputs. CatCh can be activated by blue light and ChrimsonR is sensitive to both orange and blue light, therefore, synaptic responses to ChrimsonR were evoked by a single pulse of orange light (1 ms) with full-field illumination through the 60x objective. We found that prolonged stimulation of orange light drives ChrimsonR into the desensitized state and causes depolarization block of the pre-synaptic terminals, rendering it transiently unresponsive to blue light.[48] Therefore, the response to CatCh was obtained by delivering blue light stimulation (0.2 ms) immediately following 250 ms of orange light illumination. oEPSC amplitudes were obtained from average traces of 3–5 trials.

QUANTIFICATION AND STATISTICAL ANALYSIS

Analysis of *in vivo* electrophysiology data

Spike sorting was performed using default parameters in Kilosort2.[79] Kilosort outputs were manually curated in Phy (github.com/kwikteam/phy). Single unit responses to gratings were quantified by measuring the mean firing rate (F0) in response to all unique combinations of spatial frequency and direction. To determine if units were visually responsive, responses to blank gray screen trials were compared with responses from the spatial frequency/direction combination that elicited the largest response. A Mann-Whitney test was performed on responses to blank trials and preferred trials and units were classified as visual if $p < 0.01$. The preferred spatial frequency was determined by first measuring the direction that elicited the largest response. The spatial frequency that elicited the largest responses at the preferred direction was used as the preferred spatial frequency for each unit.[82]

To determine response reliability, a quality index (Qi) was computed as previously described.[89] Spiking responses were segmented into 0.1 s bins to form a Trial x Response matrix, representing responses to the optimal frequency/direction gratings for each unit over multiple trials. Qi was calculated by dividing the variance of the mean response by the mean variance across trials. Units with a Qi less than 0.25 were excluded.

To assess unit stability before and after optogenetic stimulation trials, F0 responses from the preferred spatial frequency/direction combination were compared using a Mann-Whitney test. Units were excluded if F0 responses significantly differed ($p < 0.05$) after optogenetic stimulation trials. Additionally, Qi was measured by combining trials before and after optogenetic stimulation trials. Therefore, units that had significantly different responses after optogenetic stimulation were also excluded based on Qi (see above).

To estimate the depths of specific recording sites within the dLGN, animals were presented with contrast modulated white noise movies.[28,73] Spike triggered averaging was performed on frames of the movie that occurred 50 ms prior for every multi-unit spike recorded on each recording site. Because multi-unit receptive fields shift along the ventral-dorsal axis of the electrode tract in dLGN, sites with clearly defined receptive fields were used to determine the normalized depth of each recording site within the dLGN.

Axis-selectivity index (ASI) was computed as $(R_{preferred} - R_{orthogonal}) / (R_{preferred} + R_{orthogonal})$, where $R_{preferred}$ is the mean response to gratings moving along the cell's preferred axis. $R_{orthogonal}$ is the mean response to gratings moving along the axis orthogonal to $R_{preferred}$. Direction-selectivity index (DSI) was computed as $(R_{preferred} - R_{opposite}) / (R_{preferred} + R_{opposite})$. $R_{preferred}$ is the mean response to gratings moving in the cell's preferred direction (i.e. the direction that elicits the largest response). $R_{opposite}$ is the response to gratings moving in the opposite of $R_{preferred}$. Units with an ASI > 0.33 and DS < 0.33 were classified as AS; units with DSI > 0.33 were classified as DS; and units with DSI < 0.33 and ASI < 0.33 were classified as broadly-tuned. Units that exhibited responses that were significantly reduced by gratings were classified as Sbc.

ON-OFF index of units in response to full-field flashes was computed as follows: $(R_{ON} - R_{OFF}) / (R_{ON} + R_{OFF})$. R_{ON} and R_{OFF} represent the mean firing rate of each unit calculated during the first 400 ms following light onset (R_{ON}) and offset (R_{OFF}). Units with an ON-OFF index greater than 0.33 were classified as ON; units with an ON-OFF index less than -0.33 were classified as OFF; and units with an ON-OFF index between -0.33 and 0.33 were classified as ON-OFF. Gratings Preference Index was computed using the equation: $(R_{fine,\ slow} - R_{coarse,\ fast}) / (R_{fine,\ slow} + R_{coarse,\ fast})$. $R_{fine,\ slow}$ and $R_{coarse,\ fast}$ represent the mean firing rate of each unit in response to 0.16 c/d and 0.04 c/d, respectively.

Tests of multimodality were performed using the Hall and York calibration of Silverman's critical bandwidth test where the null hypothesis is that the distribution has a single mode and the alternative is there is more than 1 mode. Each test used 5000 bootstrap samples from the sample data and calculated the critical parameter h. The p value was approximated by comparing the bootstrap results to a 500 sample Monte-Carlo simulation where each sample was taken from a normal distribution and 5000 bootstrap samples were taken from each of those samples.

To quantify responses to optogenetic activation of RGC axons, we binned spiking responses to optogenetic stimulation into 0.5 ms intervals to create a peristimulus time histogram. The interval with the highest number of spikes within 10 ms of the optogenetic stimulus onset was used to measure synaptic delay. To calculate opto-spike efficiency, we summed the number of spikes in the peak interval with those in the adjacent intervals, divided this sum by the total number of light pulses (50), and multiplied by 100 to convert to a percentage. This analysis was performed for each pulse in the 5 Hz pulse train, and the pulse with the highest opto-spike

efficiency was used to determine the opto-spike efficiency for each unit (referred to as "max opto-spike efficiency). Typically, the first pulse in the 5 Hz pulse train elicited the most reliable spiking (Figure S1).

Two-photon calcium imaging of ooDSGCs

Analysis of ooDSGC responses to drifting gratings was performed on retinas used in our previously published dataset characterizing RGC types labeled in *Cart-IRES2-Cre* mice.[20] A subset of ooDSGCs from this dataset were presented with both moving bars and drifting grating stimuli matching those used for *in vivo* dLGN recordings. Full-field drifting gratings moving in 8 different directions were presented for 4 s with an interstimulus interval of 5 s. Drifting gratings consisted of two different spatial frequencies (0.04 and 0.16 cycles/degree) with a temporal frequency of 2 Hz. Each unique direction and spatial frequency combination was presented 4 times in pseudorandom order. Of the 246 ooDSGCs that were classified using moving bars in our previous study, 38 were presented with drifting gratings. Responses of these cells were further analyzed.

DSI was computed using the same equation used for dLGN neuron responses: $(R_{preferred} - R_{opposite}) / (R_{preferred} + R_{opposite})$ with $R_{preferred}$ being the mean response to gratings moving in the cell's preferred direction and $R_{opposite}$ being the response to gratings moving in the opposite of $R_{preferred}$. Max responses in response to each stimulus are the peak $\Delta F/F_0$ to bars or gratings moving in the preferred direction for each cell.

Quantification of axonal projection patterns in the dLGN

Maximum intensity projection images of dLGN sections were outlined in ImageJ using the Kcng4-Cre labeled signal as a reference. The images were then rotated so that the intergeniculate leaflet lay horizontal. The projection images were subtracted by the pixel value three standard deviations above the mean pixel value in the posterior thalamic nucleus. A median filter with a radius of 1 pixel was applied to remove noise. The image was then binarized, assigning a value of 1 to any remaining pixel with a value greater than 0. The reoriented dLGN was then bounded by two curved lines drawn on the dorsal and ventral borders of the dLGN, with the dorsal line excluding the optic tract. Pixels with equal horizontal distance to the drawn dorsal border were summed, sampling every fourth row to avoid overcounting large structures. Rows shorter than 250 μm were excluded to minimize skew for distances near the dorsal border. The resulting sums were averaged from two images each from five animals, for anterior, mid, and posterior sections, respectively, and plotted as a function of distance from the dorsal border.

Analysis of slice electrophysiology data

Contribution index (CI) is calculated by dividing the difference between the responses of Kcng4-Cre$^+$ and ProD1$^+$ inputs to their summed response: $(R_{ProD1} - R_{Kcng4}) / (R_{ProD1} + R_{Kcng4})$ with R_{ProD1} and R_{Kcng4} representing the peak amplitude of AMPAR oEPSCs evoked by ProD1$^+$ and Kcng4-Cre$^+$ inputs, respectively. Values larger than 0.9 or smaller than -0.9 identify predominant (95%) contribution from ProD1$^+$ or Kcng4-Cre$^+$ RGC inputs, respectively.

Data calculation and statistical analysis were conducted using Graphpad Prism. All data sets were evaluated for normality using the Kolmogorov-Smirnov test. For nonparametric distributions, the two-sided Wilcoxon signed rank test were used for paired comparison. For normally distributed data sets, the paired two-sided t test was used. For all figures, $^*p < 0.05$; $^{**}p < 0.01$; $^{***}p < 0.001$.